Drizzle in stratocumulus clouds. Part I: Aircraft observations

Robert Wood*
Met Office, Meteorological Research Flight & Farnborough, UK

November 25, 2001

Abstract

Detailed observations of stratocumulus clouds on twelve days are examined with specific reference to drizzle formation processes. The clouds differed considerably in thickness, liquid water path and droplet concentration. Cloud base precipitation rates contents differed by a factor of 20 between cases. The lowest precipitation rate was found in the case with the highest liquid water path and highest droplet concentration suggesting that drizzle can be severely repressed in polluted clouds.

mention effect on adiabaticity and variability

The vertical distribution of cloud liquid water and microphysical parameters is examined in detail. In general, the highest concentration of $r > 20\mu$m drizzle drops is found towards the top of the cloud and the mean volume radius of the drizzle drops increases monotonically from cloud top to base. The resulting precipitation rates are largest at the cloud base but decrease markedly only in the upper 40% of the cloud. Layer averaged drizzle drop size distributions are shown to be well modelled by an exponential distribution. Below cloud, precipitation rates decrease with distance below base. The decrease is considerably less than that found using a simple sedimentation-evaporation model, suggesting turbulence may play an important role in the redistribution of drizzle drops below cloud. In addition, the observations suggest that much of the drizzle flux at cloud base is evaporated within 150-250 metres below cloud base, which in many cases limits the dynamical effects of drizzle to the moistening and cooling of the subcloud layer rather than in removal of moisture from the boundary layer.

The sample volume limitations of the 2D-C probe for large drizzle droplets is assessed and it is shown that estimates of the higher moments (radar reflectivity) are biased significantly only when precipitation rates are high. Radar reflectivity-precipitation rate relationships are explored using the *in-situ* microphysical measurements which may prove helpful for the radar remote sensing of drizzle. The microphysical measurements are also used to validate several parameterizations of autoconversion, accretion and sedimentation. Some marked differences were found in the autoconversion formulations. The parameterization by Khairoutdinov and Kogan is found to best represent the drizzle processes in stratocumulus clouds.

Keywords: stratocumulus, drizzle production, coalescence, turbulence

1. Introduction

The production of drizzle in warm stratiform clouds is a potentially important climatological process because (a) drizzle droplets are ubiquitous in stratiform boundary layer cloud and (b) stratus/stratocumulus is the dominant cloud type over large areas of the ocean. The effect of drizzle upon the cloud liquid water path, the hydrological cycle and the structure and stability of the boundary layer is not well known because of the difficulty in coupling accurate size-resolved microphysical models with high-resolution dynamical models. There is little doubt that accounting for turbulent redistribution of droplets within boundary layer stratiform clouds is necessary to obtain realistic drizzle precipitation rates (Nicholls 1987, Austin et al. 1995). In the simulations of Nicholls (1987), realistic levels of turbulence were included using a transilient matrix technique (Stull 1984). It was found that the turbulence, by allowing large drops to be maintained for longer within the cloud, vastly increased the concentration of large drops throughout the cloud. Although the turbulence levels in Nicholls' simulations were modest (vertical wind standard deviation 0.09$< \sigma_w <$0.72 m s^{-1}). the results suggest that parameterizations of drizzle formation in boundary layer clouds would be incomplete and inaccurate without accounting for the turbulence intensity.

Recent work has suggested other mechanisms for promoting drizzle production. Feingold et al. (1999), used a suite of microphysical and dynamical models, including large-eddy simulations with explicit microphysics, to show that the inclusion of realistic numbers of giant haze particles could increase the amount of drizzle liquid water content. The effect is more marked when the background drizzle rate (the drizzle rate without the

*Corresponding author current affiliation: Atmospheric Sciences, University of Washington, Seattle, WA 98195, USA. Email: robwood@atmos.washington.edu

inclusion of giant haze particles) is low. For example, in simulations of a 450 m thick stratocumulus cloud with a droplet concentration of 250 cm^{-3}, the addition of 10^{-2} cm^{-3} haze particles with radii of 20 μm increased the drizzle liquid water content by more than an order of magnitude. Such concentrations of large haze particles (which contain predominantly sea-salt) can be produced at the sea surface by whitecapping under high wind speed conditions (Monahan et al. 1986). If the cloud layer is close to the surface then there is a greater chance that these particles will be assimilated into the cloud and take part in the collision-coalescence process. It is important therefore to be able to quantify the magnitude of this effect at different wind speeds.

Another important issue is that the drizzle in stratocumulus clouds tends to occur in intermittent patches (Austin et al. 1995). These patches may occur in regions where the cloud thickness is significantly greater than the mean cloud thickness of the layer as a whole. Thicker regions of cloud will have larger droplets and higher liquid water contents near cloud top than thinner regions and the relationship between cloud thickness and coalescence rate is thought to be strongly nonlinear (Nicholls 1987, Austin et al. 1995). The mean drizzle precipitation rate produced by a cloud with a thickness equal to the mean thickness of the cloud is likely therefore to be lower than the drizzle rate produced by the inhomogeneous cloud. This leads to a biased precipitation rate if, in a GCM, grid-box mean values are used to estimate the precipitation rate (Larson et al. 2000; Wood et al. 2000). We examine the likely magnitude of these biases in this study.

The study is composed of two parts. In part I we describe observations of drizzle in stratocumulus clouds that have been obtained using the Met Office C-130 research aircraft in 12 stratocumulus cloud sheets. Eleven of the flights were flown over the Atlantic Ocean and North Sea around the UK. The other flight examined was flown as part of the ASTEX Lagrangian 1 suite in the Azores region of the Atlantic Ocean. All flights were flown specifically to obtain extensive observations of the vertical structure of the cloud deck. The clouds examined have a considerable variety of droplet concentrations, liquid water paths and drizzle production rates which allows us to make inferences about (a) the role of droplet concentration and liquid water path upon the production of drizzle and (b) the effects of drizzle upon the depletion of liquid water content in stratocumulus clouds. Part II of the study presents a model study of the drizzle formation process in which the observations provide validation for two types of model, which differ considerably in their complexity. The first type of model is a bin microphysical multi-layer model similar to that of Nicholls (1987) and Austin et al. (1995) which takes as inputs the observed cloud droplet size distributions (droplets with radii smaller than 20 microns) and solves the stochastic collection equation at each level to generate an equilibrium drizzle droplet size distribution. The effects of sedimentation, turbulent redistribution, condensational and radiative growth of drizzle droplets are included. The second model type is a much simpler multi-level model in which the drizzle is represented by a single variable (the drizzle liquid water content) at each level. As with the bin-microphysical model, the cloud droplet size distribution is used to initialise the simulations. However, only two moments, the liquid water content and the droplet concentration, are used. The drizzle water content is generated using simple autoconversion and accretion formulations. Sedimentation is simulated using a sedimentation rate-drizzle water content relationship derived from observations. The effects of condensational and radiative cooling growth of drizzle droplets is not included. This type of model is closer to models typically used to model rain growth in large-scale numerical models.

This paper examines the role of turbulence, large haze particles and cloud thickness variability in the production of drizzle within stratocumulus layers. We compare aircraft observations of stratocumulus with results from a 1-D bin microphysical model which includes the effects of turbulent mixing and large sea-salt particle production. By running a number of simulations for each case, we examine the effect of a variable cloud thickness upon the mean precipitation rate. Section 2 presents details of the numerical model formulation. In section 3 aircraft observations are described and presented. In section 4 we present a detailed comparison of the aircraft observations and the numerical model. We conclude our findings in section 5.

2. Case details

a. Flights

All aircraft data were collected using *The Met. Office* C-130 aircraft in stratus and stratocumulus clouds. Twelve flights are presented in this study. Eleven of the flights took place during the day over the oceanic waters around the United Kingdom. One flight (A209) was flown at night as part of the ASTEX 1st Lagrangian experiment in the Azores region of the Atlantic Ocean. Table 1 presents details of the flight numbers, locations, times, mean cloud base and cloud top height, mean liquid water path, mean droplet concentration and mean cloud base precipitation rate. In this the different cases will be referred to by flight number. There is a considerable range of mean liquid water path (45-360 g m^{-2}), droplet concentration (8-420 cm^{-3}) and precipitation rate (0.046-2.90 mm day^{-1}) between flights which will allow inferences to be made as to the dependence of drizzle formation upon cloud bulk and microphysical parameters.

The sampling strategy differed between flights, although in each case there was good sampling of the vertical and horizontal structure of the cloud. In all flights the mean aircraft position followed an approximately lagrangian path, drifting with the mean wind in the boundary layer (as deduced from real-time aircraft measurements), which limits analysis problems associated with advection. Flights consisted of a series of straight and level runs, in, above and below cloud, together with a number of vertical ascents from above cloud to the surface ($\sim$ 15 m). Many of the flights were augmented with a series of sawtooth runs up and down through the cloud (from approximately 100 m below to 100 m above cloud), to give enhanced vertical sampling of the cloud. The total number of ascents/descents through cloud varied from 3 (A209) to 43 (A693). At least one ascent on each flight characterised the atmosphere from cloud top to $\sim$6000 m. Where possible a run was carried out at the lowest possible flight altitude ($\sim$ 30 m) to characterise the lower boundary conditions. The straight and level runs were typically 60 km in length, but on flights A648 and A649 a greater number of shorter runs were used (20 km). The total length of horizontal flight legs allowed reasonable turbulence statistics to be derived from the data.

b. Instrumentation and data analysis methods

Instrumentation to measure dynamic (wind components) and thermodynamic (humidity, liquid water content) variables is described in more detail in Rogers et al. (1995). Cloud microphysical measurements were made using a PMS (Particle Measuring Systems) Forward Scattering Spectrometer Probe (FSSP) which counts and sizes particles into 15 size bins in the radius range 1-23.5 μm. Larger particles were measured using a PMS 2D-C optical array probe which counts and sizes particles into 32 size bins in the radius range 12.5-400 μm. For the 2D-C data the first size bin is not used as there is large uncertainty in the sizing of particles in this bin (Korolev et al. 1998). Combined FSSP and 2D-C size distributions are produced by linear interpolation in log(dN/dr)-log(r) coordinates. To facilitate comparison with the model size distributions, the observed spectra are interpolated onto the model radius bins (logarithmically spaced in radius). Sea surface temperature was measured using a Heimann nadir-pointing radiometer and was corrected for absorption between the surface and the lowest flight level using the method of Hignett (????).

Turbulent variance and covariance flux measurements were derived from the data using by first detrending the time series by removing a 3 km wide running mean and then using eddy correlation. This removes effects caused by erroneously drifting sensor outputs and transports caused by motions significantly larger than the largest turbulent eddies.

c. Case details and overviews

All four flights described in this paper took place over the sea around the UK. Table 1 gives details of the dates and locations, together with some mean properties of the clouds measured. Most of the flights took place between the hours 11 UTC and 16 UTC. It is clear that there is a considerable range of droplet concentrations (25-400 cm^{-3}) and cloud liquid water paths (45-360 g m^{-2}) between the flights. The liquid water paths LWP were calculated using a number of ascents/descents through the cloud layer. This method of estimating liquid water path is prone to bias because the aircraft does not make a vertical passage through cloud, but instead moves with an ascent/descent rate of approximately $\pm$3 m s^{-1}. For a 300 m deep cloud the horizontal distance travelled between cloud base and cloud top is some 10 km at a science cruising speed 100 m s^{-1}. However, when calculating a mean value of LWP the degree of bias becomes less as the number of ascents increases. We carried out simple tests using a hypothetical cloud with a sinusoidal cloud base height and constant cloud top. This allowed us to estimate the degree of uncertainty in our estimated value of $\overline{LWP}$. Droplet concentration is measured using the Forward Scattering Spectrometer Probe (FSSP, see e.g. Baumgardner et al. 1993). The number of droplets with sizes larger than the maximum measurable by the FSSP (23 μm radius) does not contribute significantly to the total in-cloud droplet concentration in any of the cases. We calculate the mean droplet concentration using all 10 second samples in the height range $0.33 < z_* < 0.67$ to avoid sampling regions close to cloud base and cloud top. The error in the mean is then $\sigma_{N_d}/sqrt(N)$ where N is the number of samples. For all flights this error is very small ($<$ 5 cm^{-3}).

Also given in Table 1 is the mean cloud base precipitation rate. We define z_* as a normalised height given by

$$z_* = \frac{z - \overline{z_{CB}}}{\overline{z_i} - \overline{z_{CB}}} \tag{1}$$

where $\overline{z_{CB}}$ and $\overline{z_i}$ are the mean cloud base height and cloud top respectively and z is the height of a particular measurement. Because it is not possible to assign a local cloud base to every measurement, it is possible due to the spatial and temporal variability in the cloud geometrical properties that a measurement at height z could be either above or below cloud base when $z_* = 0$. We calculate the cloud base precipitation rate as being the average precipitation rate in the region $0 < z_* < 1/3$. For a given cloud particle size distribution, the precipitation rate P is calculated from

$$P = \frac{4}{3}\pi\rho_w \int_{r=0}^{\infty} w_T(r)\frac{dN}{dr}r^3 dr \tag{2}$$

where $w_T(r)$ is the terminal velocity of a droplet of radius r, $\frac{dN}{dr}$ is the number of droplets in the size range r to $r + dr$, and ρ_w is the density of liquid water. Values of w_T as a function of size are calculated using the Reynold's number-Best number method as described in Pruppacher and Klett (1997). We calculate P only over the radius range $20 < r < 400\mu$m. There were no drops measured larger than 400μm. Interestingly, droplets smaller than 20 μm can contribute considerably to the precipitation rate, but the fall speeds are so small ($w_T \approx$ 5 cm s^{-1} for $r = 20\mu$m falling to just over 1 cm s^{-1} for $r = 10\mu$m) that it would take 8 hours for a 10 μm droplet to fall through a 300 m thick cloud. Turbulent effects therefore are much more important at determining the trajectories of droplets smaller than $\sim$ 20 μm.

Dynamic and thermodynamic parameters for the cases are given in Table 3. The SST was calculated from a run at the lowest flight level. Typical errors are of the order 0.4 K. The wind speed U_{10} at a height of 10 m is estimated using the mean wind speed at the lowest flight level (100 m in all cases) and extrapolating this measurement down using a logarithmic wind profile (e.g. Bretherton et al. 1995) and a roughness length of $5{\times}10^{-4}$ m (suitable for oceanic conditions, Stull 1988). The friction velocity is estimated using the u and v momentum fluxes from the lowest flight leg ($\sim$ 30 m in all cases). The friction velocity scales quite well with U_{10} using the Charnock (1955) relation with $c = 11.0$ (see Nicholls and Readings 1979), apart from at low wind speed ($U_{10} <$ 3 m s^{-1}) where the observed friction velocities exceed those from Charnock's relation. The convective velocity scale w_* is calculated using the buoyancy integral method (e.g. Deardorff 1980) as described in Nicholls and Leighton (1986). We use the bouyancy integral over the entire boundary layer from the surface to cloud top. In some cases the buoyancy integral was negative due to low buoyancy generation in cloud or because the air was being cooled by a lower SST so that negative subcloud virtual potential temperature fluxes were produced. In these cases the w_* could not be defined. Turbulent kinetic energy (TKE) in the boundary layer is generated by buoyant generation, shear generation or a mixture of the two. In boundary layers driven predominantly by shear generation observations suggest that the vertical wind variance scales well with u_* (see e.g. Nicholls and Leighton 1986) and we also find this for cases A644, A648 and A762. A measure of the relative roles of shear and surface buoyancy production of TKE is given by the ratio of the boundary layer depth z_i to the Monin-Obukhov length L_{MO}. Large positive values of $-z_i/L_{MO}$ indicate that turbulence is driven primarily by thermal convection. Small negative values that shear generation of turbulence dominates. Our definition of L_{MO} accounts for the fact that cloud top cooling in addition to surface forcing can be an important source of buoyancy generation, so we define as

$$L_{MO} = -z_i \frac{kw_*^3}{u_*^3} \tag{3}$$

where $k = 0.4$ is the Von Karman constant, and w_* is defined using the buoyancy integral as mentioned above. Positive values of L_{MO} are possible because the bouyancy integral can be negative. Table 3 shows that flights A049, A209, A439, A641, A649, A764 and A767 are all dominated by buoyancy generation, with the other flights being driven primarily by shear production.

Also presented are the mean in-cloud vertical wind standard deviation $\overline{\sigma_w}$, which tends to be larger in the convectively driven cases. To assess the role of radiation in generating cloud turbulence we simulate radiative transfer through the clouds using a four-stream radiative code (Edwards and Slingo, ref???). Long-wave flux divergences across the boundary layer as shown in Table **??** are all negative (net loss) and range from around -50 W m^{-2} in cases with relative cold cloud tops and moist lower tropospheres, to -85 W m^{-2} in summer cases with low moisture above the boundary layer. In contrast, the short-wave flux divergences are strongly modulated by the solar zenith angle. Because all of the flights were flown at approximately the same local time each day (apart from A209 which was at night), this results in a strong winter-summer difference in short-wave flux divergence, with relatively little absorption for the winter cases (maximum 21 W m-2) to values comparable to, or even greater than the magnitude of the long-wave flux divergence. For all the winter cases this results in a net loss of radiation of 30-45 W m^{-2}. The net gain/loss in the daytime summer cases is much smaller (net losses between -7 to 24 W m^{-2}).

Both long-wave cooling rates and short-wave heating rates are largest at cloud top but the decay distance is much smaller for the long-wave cooling rates which results in a sharp net cooling from the cloud top to a few tens of metres below cloud top and a weaker warming through the remainder of the cloud. Because the cloud base temperature is generally colder than the surface temperature, there is a small additional long-wave heating close to the base of the cloud. This warming/cooling profile can destabilise the cloud layer (refs???) and through effects upon the vertical distribution of the sensible heat flux can lead to a decoupling of the cloud layer from the surface. Only two cases had cloud layers that were clearly decoupled from the surface layer (A649 and A767). The reasons for decoupling in A649 (with a mixed layer base at $z \approx$ 200m) are difficult to determine but in A767 a high surface latent heat flux (110 W m^{-2}) was promoting a warming-deepening form of the decoupling (Wyant and Bretherton 1997) as the air mass had moved southwards from the Arctic over the previous two days. Cumulus clouds were observed to form at the top of the surface layer ($\approx$ 600m) and in places penetrated the overlying stratocumulus layer. The other summer case boundary layers remained coupled because of the shallow boundary layers.

The cloud and boundary layer observed in cases A644 and A648 were markedly different in nature to the other cases. Both cases were formed in moist airmasses moving northeastwards from the Azores region over colder seas. The surface heat fluxes in these cases were negative and a shallow (200 m deep) shear-driven mixed layer was present. Above this layer the temperature exhibited a stable lapse rate (2-3 K km^{-1}) up to around 800-1000 m. Patchy layers of cloud were present at most levels in this layer. Above this layer the temperature profiles indicate a moist adiabatic lapse rate which contained less cloud than the stable layer below. This layer was capped with a weak inversion (1-3 K) at 1800-2000 m (A644) and 1400-1600 m (A648) with layer cloud beneath. Back-trajectories calculated using the Met Office NAME trajectory model (ref???) suggested that the lower tropospheric air had been subjected to large-scale ascent in the 24 hour period prior to the observations taken on flights A644 and A648. This ascent was most likely associated with warm frontal zones which, although the surface fronts were analysed as being at least 100-200 km from the observational area, appeared to have a marked affect upon the boundary layer. There were no high or mid level clouds during A644 and some patchy altocumulus layers during A648. The ascent rates for the 24 hour period prior to the observations were estimated as 0.9 and 0.8 cm s^{-1} for A644 and A648 respectively, although the trajectories suggested no large-scale ascent on A644 during the observational period, and subsidence during the observational period on A648.

The mean in-cloud vertical wind integral scale $\overline{\lambda_w}$ is calculated using the autocorrelation method of Lenschow and Stankov (1986). This is a measure of the horizontal distance over which the vertical wind decorrelates, so that large values indicate that large coherent eddies are dominant. Typically in a convective boundary layer this integral scale tends to be smallest at the surface increasing with height. We find this to be the case here. The mean in-cloud integral scale tends to be smallest in clouds capping shallow boundary layers (A693, A763 and A764 all have cloud tops lower than 500 m and $\overline{\lambda_w}$ <100 m) especially when the mixing in the boundary layer is driven largely by shear.

3. Vertical thermodynamic, cloud liquid water and microphysical structure

a. Temperature and total water content

Figure **??** profiles of mean temperature (a) and total water content (b) in the cloud layer. The temperature is referenced to the moist adiabatic temperature calculated which is calculated using the mean value of the moist adiabatic lapse rate in the cloud layer. The height variation of the moist adiabatic lapse rate from the mean value does not exceed 0.2 K km^{-1} in any of the cases and in most of the clouds it is less than 0.1 K km^{-1}. The data show that the temperature lapse rate in cloud in all cases except A644 and A648 is close to the moist adiabatic rate, which one would expect in the case of a well-mixed boundary layer where the entrainment rate is small ($w_e/w_* \ll 1$). The Rosemount E102AL total temperature sensor used on the C-130 measures air temperature with an error of approximately 0.2-0.5 K. Coupled with the additional problems of possible sensor wetting in cloud , the overall uncertainty in temperature is too large to determine deviations from adiabaticity in the well-mixed cases except close to cloud top where the effects of entrainment are seen. The deviations in A644 and A648 are significant and highlight the considerable subadiabaticity and poor mixing in these cases.

The total water content is plotted as the mean value at each level minus the mean value for the entire cloud layer q_{T*} to facilitate comparison between cases. As with temperature all cases except A644 and A648 show small gradients in total water content with height. In cases A644 and A648 the total water content falls considerably over the height of the cloud. Low in these clouds turbulence caused by shear (in both cases $U_{10} > 9$ m s^{-1}) is transporting moisture laden air upwards. Higher in the cloud the moisture fluxes are small and insufficient to prevent loss of water through drizzle.

b. Liquid water content and droplet concentration

Drizzle production is strongly dependent upon the liquid water and microphysical cloud characteristics. To facilitate the comparison between flights we define N_* as the mean droplet concentration from all the 1 Hz samples in cloud. A sample is denoted as cloudy if the LWC measured with the Johnson-Williams (JW) hotwire probe exceeds 0.02 g m^{-3}. We choose this threshold to avoid misclassification because the JW probe is known to suffer small instrumentally-related oscillations with an amplitude of between 0.005 and 0.02 g m^{-3} even when the probe is out of cloud. In any case, we found that variation of this threshold between 0.02 and 0.05 g m^{-3} made litte difference to the derived value of N_*. These values are given in Table 1. We then calculate layer averages over a number of height bins (between 8 and 15 depending upon the vertical resolution of the measurements which differed between flights) in the range $0 < z_* < 1$. Figure **??**(a) shows the mean droplet concentration at each height bin normalised with N_* plotted as a function of z_* for each flight. Cases other than A644 and A648 all show a similar behaviour with $\overline{N_d}/N_*$ increasing with normalised height up to around z_*=0.3-0.4 then remaining approximately constant and unity up to z_*=0.8. Above this height the droplet concentrations decrease. Although it is tempting to ascribe the drop-off in droplet concentration and the cloud base and cloud top to effects of nucleation and entrainment respectively, it is important to stress that fluctuations in cloud base and cloud top heights are more responsible for the smaller means near the cloud boundaries. Means calculated using only in-cloud values show near-unity values from very close to cloud base to $z_* \approx 0.9$. Figure **??**(b) shows the standard deviation of the droplet concentration at each height normalised with the mean value at that height. Higher values are found close to the cloud boundaries due to the averaging over both cloudy and clear regions. In the cloud centre values of $\sigma_{N_d}/\overline{N_d}$ are typically 0.1-0.4 for the classical cases. These values can be compared with observations by Noonkester et al. (1984) who found that $\sigma_{N_d}/\overline{N_d}$ between 0.l and 0.2 in the cloud interior for two stratocumulus case, and increasing values towards the cloud boundaries. Large eddy simulation (Stevens et al. 1996) of a non-precipitating stratocumulus cloud led to values of $\sigma_{N_d}/\overline{N_d}$ of approximately 0.2-0.4 in the central 50% of the cloud increasing to 0.6-1.0 close to cloud base and cloud top. In contrast, the cases A644 and A648 show larger values through much of the cloud layer reflecting the broken nature of the these layers.

Nicholls and Leighton (1986) point out that deviations of a cloud layer from the adiabatic are more easily observed by looking at deviations in liquid water content from adiabatic than by looking at temperature or total moisture. We use the same formulation as Nicholls and Leighton (1986) in that we define a value $q_{ad}(z_i)$ to be the adiabatic liquid water content at cloud top, i.e. $q_{ad}(z_i) = \Gamma_{ad}(\overline{z_i} - \overline{z_{CB}})$ where $\Gamma_{ad}(T, p)$ is the adiabatic increase in liquid water content with height, a weak function of temperature and pressure. A single value of Γ_{ad} is used in each case, calculated using the mean in-cloud temperature and pressure. We then calculate the degree of subadiabaticity by calculating q_{ad} for each level, subtracting the observed mean value $\overline{q_L}$ and normalising with $q_{ad}(z_i)$. This parameter (Fig. **??**(c)) is zero for a fully adiabatic cloud and equal to z_* for cloud free conditions. The clouds range from close to adiabatic (A648) to very subadiabatic (A644, A648) with a broad range in between. Parameters that can affect the degree of adiabaticity are drizzle loss (Stephens et al. 1998) and the balance between the transport of moisture through the cloud boundaries and the efficiency with which turbulent motions can redistribute the moisture through the layer (Wyngaard and Brost 1984, Nicholls and Leighton 1986). Finally, Fig. **??**(d) shows the ratio of the standard deviation of the liquid water content to the mean in the layer as a function of normalised height. This typically decreases through the lowest 2/3 of the cloud before increasing again as the upper boundary is reached.

All clouds with the exception of A641 have distinctly subadiabatic liquid water contents throughout most of the cloud layer. The cases A644 and A648 are highly subadiabatic. The effects of a variable cloud top and entrainment on mean liquid water contents can be seen above $z_* = 0.8$ where the gradient of $(q_{ad} - q_L)/q_{ad}(z_i)$ increases considerably. For most of the cases the gradient in the range $0.2 < z_* < 0.8$, away from the cloud base and top, is approximately constant which indicates that the ratio of the liquid water content at a level to the adiabatic value at that level is constant. Note that a rate of change with normalised height in $(q_{ad} - q_L)/q_{ad}(z_i)$ of 0.4 is equivalent to a difference in total water content across the cloud layer of only around 0.1-0.3 g kg^{-3}, which is close to the accuracy of the total water probe.

Values of $\sigma_{q_L}/\overline{q_L}$ (Fig. **??**(d)) decrease from between 0.5-1.5 close to cloud boundaries in the well-mixed cases to 0.2-0.5 in the cloud interior, similar to the LES simulations of Stevens et al. (1996). Much of this variation reflects the horizontally varying cloud base height rather than variations in the degree of adiabaticity from region to region. This can be deduced by considering the horizontal variation in q_L that one would expect given a particular variation in cloud base. We discuss this further in section ????.

We carried out a more detailed study of the subadiabatic nature of the clouds by looking at each profile individually. In this way, effects of fluctuations in cloud base and top, which contaminate the profiles in Fig. 3 near the cloud boundaries, are reduced. For each profile we estimate cloud base and height from both the droplet concentration measurements and the liquid water content measurement. The two estimates of the cloud boundaries we found to be within 20 m in 85% of cases and within 50 m in all cases. We then calculate the adiabatic liquid water path for each profile as $LWP_{ad} = (1/2)\Gamma_{ad}(z_i - z_{CB})^2$, where Γ_{ad} is calculated using the mean temperature and pressure in the cloud layer. We estimate the liquid water path from the observed profile by simple integration of the observed q_L. The ratio f_{ad} of the observed to adiabatic LWP is thus estimated for each profile. The mean of these values for each flight is given in Table 2. We estimate the error in mean LWP using profiles through a hypothetical cloud where the local liquid water content is a linear function of height above the local cloud base. The cloud has a sinusoidal cloud base and flat cloud top. The amplitude of the sinusoid is taken from the observations of cloud base height. The horizontal wavelength is taken to be 20-40 km, a typical lengthscale for cloud base fluctuations in stratocumulus clouds. Each individual profile can result in a biased LWP because of variations in cloud base. Given enough profiles for each case this method results in an unbiased estimate of the cloud LWP and f_{ad}. The errors increase as the horizontal wavelength increases and decrease as the number of profiles increases. The error in f_{ad} is shown in Table 2. This error does not include unknown systematic errors in the JW liquid water content sensor used to make the measurements, but these are likely to be smaller than 10%.

Figure 4 shows for two cases (A641 - 20 profiles; A763 - 25 profiles) the mean ratio q_L/q_{ad} of observed to adiabatic liquid water content as a function of normalised height using the individual profile method. Both cases show a near-constant value of of adiabaticity through the bulk of the cloud ($0.2 < z_* < 0.9$) with a fall-off due to entrainment for $z_* > 0.9$. Values close to cloud base are more prone to error because of the small values of liquid water content there. The results suggest that the cloud in A641 is almost completely adiabatic and that the liquid water content in A763 is roughly 60-70% of adiabatic. This is reasonably consistent with the values in Fig. 3 which show normalised height gradients of $d((q_{ad} - q_L)/q_{ad}(z_i)/dz_*$ of ≈ 0 and ≈ 0.4 respectively in the bulk of the cloud (note that $q_L/q_{ad} = 1.0 - d((q_{ad} - q_L)/q_{ad}(z_i)/dz_*)$. We are fairly confident about adiabaticity values in most of the clouds (see estimated errors in Table 2), but the cause of the variability among the different cases is more difficult to pin down, and we discuss this further in section (???).

c. Cloud fraction

Figure 5 shows the cloud fraction as a function of normalised height for all the cases. Cloud fraction in all cases except A644 and A648 is obtained from the 1Hz FSSP droplet concentration using a threshold of 5 cm^{-3} to define the presence of cloud (Wood and Field (2000)). This threshold concentration is appropriate because it is several times higher than the highest super-micron aerosol concentrations but also substantially smaller than typical cloud droplet concentrations. Because the droplet concentrations in A644 and A648 were in places very low (¡ 10 cm^{-3}) we chose to use the JW liquid water content with a threshold of 0.02 g kg^{-1}. We chose the FSSP over the JW in the other cases because of its faster response time.

In all the well-mixed cases there is near total cloud cover (cloud fraction ¿ 0.9) in the range $0.3 < z_* < 0.8$ with a drop-off to 0.4-0.8 at the mean cloud base and top. The cases A644 and A648 show less than total cloud cover at all levels. The largest cloud fractions (0.6-0.8) in these cases are found at $z_* < 0.5$, a minimum in cloud fraction at occurs at intermediate levels, and a second peak in cloud fraction is observed around $z_* = 0.8 - 0.9$. It is interesting that the frontal cases both show a two-layer cloud structure. Very low accumulation-mode aerosol concentrations (10-20 cm^{-3}) were observed in the clear region between the layers and above cloud in both cases, suggesting that depletion of aerosol through heavy drizzle may be rendering the upper cloud deck colloidally unstable. Large eddy simulations of the A648 case (Wood, Ghosh and Jonas 2001) show that the lower cloud layer may have resulted from the moistening and cooling of the boundary layer caused by evaporating drizzle from the upper level. That a two-layer structure is observed in both frontal cases could suggest that the responsible processes could be a common feature of warm, clean stratus in ascent regions close to fronts.

d. Vertical wind

The vertical wind standard deviation σ_w is important for mixing in the cloud. Figure 6(a) shows profiles of σ_w as a function of normalised height in cloud for the different cases. In the buoyancy-driven cases this is relatively constant with height in the cloud layer. Shear-driven cases particularly A762, A644 and A648 show a general decrease in σ_w with height reflecting that the turbulence is driven primarily by surface friction. Figure 6(b) shows profiles of the vertical wind integral scale, which varies considerably between cases, and also with height in some of the cases. Lenschow and Stankov (1986) find that in convective boundary layers driven by surface heating the integral scale increases with height away from the surface. Clearly it seems reasonably intuitive to find eddy sizes becoming smaller towards fixed boundaries. However, for turbulence generated near cloud top as in the case of radiatively driven stratocumulus, the inversion does not impose a rigid lid to the turbulent eddies, although one would suspect it to dampen considerably the larger eddies resulting in smaller integral scales. However, short-wavelength gravity waves that may occur in the stable inversion layer cannot be distinguished from turbulent eddies when deriving integral scale using autocorrelation, it is unclear what we would expect. Our results do not appear to show any consistent height trends in the integral scale. [Compare with other measurements in Sc]. As noted in section ??? shear-driven turbulence generally results in smaller eddies.

Vertical wind standard deviation has been shown to be important in the production of drizzle (Nicholls 1987; Austin et al. 1995). Stronger turbulence can increase the recycling of drizzle drops in thin cloud layers resulting in huge increases in the number of large drizzle drops. This will have important consequences for the evaporation rates below cloud and in determining how much of the precipitation present at cloud base will reach the surface. The integral scale can also have considerable consequences for the transport of drizzle drops in cloud. Smaller eddies result in slower plume broadening which for falling droplets may result in less efficient recycling. We examine the effects of turbulence further in part II.

e. In-cloud microphysics

All cases contain drizzle-sized droplets, in this study defined as droplets with radii larger than 20 μm. We choose this size as a partition as it represents the crossover radius where, at typical supersaturations found in boundary layer clouds, condensation growth, the dominant process for the growth of small cloud droplets, becomes less effective than growth by coalescence (e.g. Jonas 1996). Precipition rates in 2-3 km thick warm Hawaiian rainband clouds can be as high as 20 mm hr^{-1}. At these rates the effect of precipitation has a marked effect upon cloud dynamics and structure through evaporative cooling below cloud base and depletion of cloud water. What is much less clear is the effect that precipitation has upon the dynamics of shallower stratocumulus clouds. Jensen et al. (2000) present observational evidence that evaporation of drizzle patches can generate cold microfronts akin to, albeit much weaker than, microburst density currents from thunderstorms. Jensen et al. showed that in a stratocumulus/cumulus case in the Southern Ocean the density current caused a local convergence region and spawned the generation of cumulus clouds beneath the stratiform deck which led to a thickening of the cloud. In a large eddy modelling study of shallow stratocumulus with heavy drizzle Stevens et al. (1998) showed a transition towards more cumulus-type circulations in the boundary layer, with weakened entrainment and depleted liquid water path.

Observations of cloud droplet ($r < 25\mu$m) size distributions in warm stratiform cloud are quite common in the literature (e.g. Noonkester, Nicholls, Liu, Boers et al. Martin et al. 1994; Brenguier 2000; Wood et al. 2001) to the point where they now form an active area of parameterisation research. Fewer detailed cases of observations of drizzle size distributions are to be found however, but there are a number of detailed studies (e.g. Nicholls; Boers et al 1996; Wood et al. 2001). Mention some more about the findings.

In general, observations of drizzle in stratocumulus clouds show that the droplet size distributions for drops larger than around 20 μm broaden towards clouds base. This is because drizzle drops form in the upper levels of the cloud, where the cloud droplets growing through condensation are largest, through the coalescence of cloud drops. These drops then fall through cloud growing larger by collecting other drizzle and cloud drops. Figure 7 shows some of the characteristics of the populations of drizzle droplets ($r > 20\mu$m) at different levels in cloud. Drizzle droplet concentrations $N_{d,D}$, liquid water contents $q_{L,D}$ and precipitations rates P are all normalised with their respective in-cloud means, which are given in Table 4.

Drizzle drop size distributions ($r > 20\mu$m) are particularly well described by an exponential distribution. To show this requires two normalising parameters. Because the small droplets do not follow the exponential distribution the drizzle drop concentrations and mean radii calculated using the $r > 20\mu$m drops are first corrected to account for the droplets smaller than 20 μm. Given an exponential size distribution of droplets larger than 20 μm, the total drizzle drop concentration N_{D*} and mean radius $\overline{r_*}$ extrapolating the spectrum to zero size are related to the respective $r > 20\mu$m values ($N_{d,D}$ and $\overline{r_{d,D}}$) by

$$N_{D*} = N_{d,D} \exp(r_0/\overline{r_*}) \quad (4)$$

$$\overline{r_*} = \overline{r_{d,D}} - r_0 \quad (5)$$

where $r_0 = 20\mu$m is the defined threshold radius for drizzle drops. We therefore normalise each size distribution using N_{D*} and $\overline{r_*}$. The exponential distribution is

$$dN/dr = (N_{D*}/\overline{r_*}) \exp(-r/\overline{r_*}). \quad (6)$$

Therefore, normalised spectra are given by $(\overline{r_*}/N_{D*})dN/dr$ and are plotted against $r/\overline{r_*}$ in Fig. 8. The universal exponential distribution $(\overline{r_*}/N_{D*})dN/dr = \exp(-r/\overline{r_*})$ is shown using the thick dashed line. There is a remarkably good adherence to the exponential form through the size range $0.5 < r/\overline{r_*} < 12$. At larger sizes there is a tendency for the normalised distributions to have higher concentrations than the exponential, but this may just reflect a slight underestimation of $\overline{r_*}$ which leads to lower normalised concentrations at small $r/\overline{r_*}$ and higher ones at large $r/\overline{r_*}$. In any case, there are a low number of spectra with $r/\overline{r_*} > 10$ which results in quite poor statistics. The median values of the normalised size distribution in each size category are within 20% of the universal exponential for $r/\overline{r_*} < 6$ and within 75% for $6 < r/\overline{r_*} < 12$. Sixty percent of all the distributions are within a factor of two of the exponential over the range $0.05 < r/\overline{r_*} < 10$, a concentration range of over four orders of magnitude. Ninety percent agree to within a factor of three over the range $0.05 < r/\overline{r_*} < 6$. This particularly good agreement suggests that drizzle drop size distributions in stratocumulus cloud can be represented faithfully using just two parameters, a finding that should aid the parameterisation of drizzle processes in large scale numerical models. In part II of this paper we examine this aspect in more detail.

f. *Sub-cloud microphysics*

So far we have been concerned with how microphysical parameters vary through the depth of the cloud. Feedbacks between microphysical and dynamical processes in boundary layer cloud depend upon both the heat and the moisture budgets in the boundary layer. Diabatic removal of moisture from the cloud through the drizzle process and subsequent evaporation below cloud base effectively leads to a heat source and moisture sink in the cloud layer and a heat sink and moisture source below it. The magnitude of the effect below cloud base is dependent upon the vertical distribution of the evaporation rate of drizzle drops below cloud. Thus, it is important to know this distribution, and how it changes with the characteristic radii of the drops. A simple model of the sedimentation-evaporation process is constructed to simulate the evaporation of drizzle drops below cloud base. In the drizzle drop size range ($r > 20\mu$m) the evaporation rate of a drop is linearly proportional to the subsaturation and inversely proportional to its radius. The constant of proportionality is a fairly weak function of temperature and pressure. We can model profiles of the size distribution $N(r,z)$ of a population of sedimenting, evaporating drops via the equilibrium relationship

$$w_T \frac{\partial N(r,z)}{\partial z} = -\frac{\partial}{\partial r}\left(N(r,z)\frac{Dr}{Dt}\right) \quad (7)$$

where w_T is the terminal velocity of a drop. We use an exponential distribution as the cloud base boundary condition and then calculate $N(r,z)$ at any height below cloud. We also assume here that the relative humidity is unity at cloud base and decreases at a rate consistent with a dry adiabatic temperature profile and constant specific humidity below cloud base. We set $N(r,z) = 0$ for all $r < 20\mu$m.

Integrations of Eqn. 7 are obtained for the temperature range 270-290 K and for cloud base $r > 20\mu$m volume radii $r_{v,D(CB)}$ from 30-55 μm, which covers the range of observations. We then calculate the precipitation rate normalised with its cloud base value as a function of depth below cloud base. We find that the rate of decrease in P with height is lower when $r_{v,D(CB)}$ is larger because the larger drops require a longer distance to fall before evaporation, and that $r_{v,D(CB)}^{2.5}$ is a very good normalising variable for height. We plot P/P_{CB} against $(z - z_{CB})/r_{v,D(CB)}^{2.5}$ for the observations and for the range of model conditions in Fig. 9. Although there is considerable spread in the observations, the modelled precipitation rate decrease below cloud base is in quite good agreement. The function $P/P_{CB} = \exp -k_{es}[(z_{CB} - z)/r_{v,D(CB)}^{2.5}]^{1.4}$ is a good fit to the observations, with k_{es} varying between 300 to 400 $\mu\mathrm{m}^{3.5}\ \mathrm{m}^{-1.4}$ for the observed temperature and pressure range. [1] The

[1] The author notes that Eqn. 7 can be solved analytically by separation of variables but that the incorporation of the exponential distribution boundary condition at $z = z_{CB}$ would lead to unwieldy mathematical solutions.

spread in observational values is a result of two main factors: (a) there is considerable variability in the cloud base height; (b) turbulent mixing in the cloud-subcloud layer can alter the drizzle drop profiles. The latter was also noted by Nicholls (1987) who compared subcloud drop distributions with the results of a numerical model. Nicholls' model assumes still air beneath cloud base and results in drop concentrations decreasing much faster with height below base than those measured. In part II of this study we examine this using a bin microphysics model that has a representation of turbulent mixing throughout the boundary layer.

We can generalise the observational results to say that around 50% of the drizzle flux in the cases studied here evaporates within 60-100 m of cloud base and 80% within 150-250 m below cloud base. We suspect that this will be a general result for drizzling stratocumulus. As such, it is more likely that drizzle will affect the dynamics through moistening and cooling of the subcloud layer than by removal of moisture to the surface. Only when the cloud base is very close to the surface will removal of moisture play a key role.

Evaporative cooling rates are estimated from the model results as a function of height and cloud base drizzle drop mean volume radius. These are shown in Fig. 10 as the cooling rate per each mm day^{-1} of cloud base precipitation rate. The dashed line shows the level of the peak cooling rate. These can be compared to the cooling rate from cloud-top radiative cooling which is usually 4-10 K day^{-1} averaged over the depth of the boundary layer. For a cloud base precipitation rate of 1 mm day^{-1} and a volume radius of 40 μm, the peak cooling rates are around 12 K day^{-1} at a distance of less than 100 metres below cloud base. The cooling rate averaged over the 300 m deep layer below cloud base is 7.6 K day^{-1}. Of course, as drizzle begins to moisten and cool the subcloud layer, the relative humidity will increase, which decreases the subsequent evaporation and therefore the magnitude of the cooling rates. If the sub-cloud layer remains well-mixed, the moistening-cooling will result in a decrease in cloud base height, the rate of which can be estimated. ???? How to do this?

4. Cloud horizontal variability

The ratio of the standard deviation to mean cloud liquid water content and droplet concentration were presented as a function of height in Fig **??**. A simple model of the cloud relates the in-cloud liquid water content variability to variability in cloud base height, assuming a constant value for the rate of increase in liquid water content with height above the local cloud base (Considine et al. 1997). Observations have shown that in many cases this provides a reasonably accurate model of cloud liquid water content variability. The model predicts that the standard deviation of liquid water content σ_{q_L} at a level entirely in cloud can be given by

$$\sigma_{q_L} = \Gamma_{eff}\sigma_{z_{CB}} \tag{8}$$

where $\sigma_{z_{CB}}$ is the standard deviation of cloud base height and Γ_{eff} is the rate of increase in liquid water content with height. It is not necessary that Γ_{eff} is the adiabatic value Γ_{ad}, only that it is constant for a particular cloud. Many of the flights here contained quite an unusually large number of profiles through cloud which allows a relatively accurate measure of the cloud base height variability.

With data taken from the profiles shown in Fig. **??** we plot the mean value of σ_{q_L} at cloud centre ($0.4 < z_* < 0.6$) against the standard deviation of cloud base height in all the cases with more than 10 profiles.

a. Subcloud temperature and humidity variability

Examination of horizontal runs below cloud reveal considerable variability in the virtual temperature and specific humidity on scales larger than 1 km. Several authors have reported measurable cooling and moistening of the subcloud layer on $> km$ scales most likely associated with the evaporation of drizzle (Paluch and Lenschow, 1991; Jensen et al. 2000). Here, we separate subcloud run time series into points containing drizzle and drizzle-free points (with a threshold $P = 0.01$ mm day^{-1}). Time series consist of 10-second means of each parameter to examine scales larger than 1 km. We then calculate the mean virtual temperature and specific humidity for the drizzle and drizzle-free regions. For all subcloud runs containing 20-80% drizzle points, we plot the virtual temperature difference between the drizzle and the drizzle-free regions against the corresponding specific humidity difference in Fig. 11. For evaporation of drizzle, assuming constant background conditions between the drizzle and drizzle free regions, the cooling and moistening are coupled, and this is shown using the dashed line. Two cases (A209 and A049) show good coupling. In most other cases the difference in specific humidity is larger than that expected with this simple assumption. Perhaps the most interesting finding is that the drizzle regions are almost universally cooler and moister than the drizzle-free regions. While these results cannot be taken as definitive proof that drizzle subcloud cooling and evaporation is taking place, it is highly suggestive. Increased entrainment in thick regions of clouds (i.e. those most likely to produce precipitation) could also lead to a possible warming and drying on the mesoscale, although we would then expect to find precipitating regions to be warmer and drier than non-precipitating regions. Opportunities to examine the reasons for and effects of mesoscale temperature-humidity correlations using detailed large eddy models are becoming available with the improvements in computational power (Stevens et al. 2002). Note that the cooling in many cases is of the order of 0.1-0.4 K. This degree of variability is comparable to, and may exceed, the the small scale turbulent variability in temperature in cloud capped boundary layers, indicating a potentially strong effect upon buoyancy.

b. Sizes of drizzle patches

Vali et al. (1998) present some of the first radar observations of spatial variability in drizzle drop populations in marine stratus clouds. They found in three cases of marine stratus that regions of high radar reflectivity is organised into cells with a dominant spacing of 1.2-1.5 times the depth of the cloud layer, but that the cells could occur with a wide range of sizes. We use data from horizontal runs (20-100 km in length) to examine drizzle cell size using the 2D-C probe. Examination of time series shows that drizzle along each run is clearly patchy in form. We use the 10 s mean (1 km horizontal scale) precipitation rate spatial series and identify regions for which the precipitation rate is larger than the median value for the run. This allows a separation into regions of less and more intense precipitation. Around 95% of these regions have horizontal scales smaller than 10 km and so the analysis is not too badly limited for the shorter runs, although there is of course a tendency to underpredict the mean cell size in these cases. A repeat of the analysis with only runs longer than 60 km revealed little qualitative difference in the distribution of cell sizes.

We subdivide runs into in-cloud and subcloud runs and plot the cumulative distributions of cell sizes for all flights in Fig. 12. There are several interesting features. First, most drizzle cell sizes are typically quite small with approximately 90% smaller than 8 km both in and below the cloud. The median cell sizes are 2-3 km. For the in-cloud data, over 99% of cells are smaller than 20 km. These facts demonstrate that drizzle production is highly localised. Second, larger cells are more common, and smaller cells less common, below cloud than in cloud. For example, cells larger than 15 km are 2-3 times more common below cloud, and this difference increases as the cell size increases. Sampling is poor above 20 km and so it is difficult to make inferences concerning the largest cells. The mean cell size for each flight ranges from 2.4 to 4.7 km. Because of the poor horizontal data resolution, these values could be larger than the true cell size because of our inability to resolve features smaller than 1 km. The frequency distribution of cell sizes is largest at 1 km suggesting that higher resolution observations would yield a considerable fraction of cells with sub 1 km scale. This may be why our values are somewhat larger than those found by Vali et al. (1998) using aircraft radar. Some of the difference may also arise due to differences in the method used to determine cell size. We do not consider the sampling volume of the 2D-C probe to be a particular limitation in our analysis. The precipitation rate is typically dominated by drops smaller than 50-60 μm. These are sampled in sufficient numbers to yield 100-1000 of these particles in each 10 s sample in regions of drizzle. It will be interesting to compare these results with those using a scanning radar.

Although there is considerable variability in precipitation rate on small scales, there is considerable modulation on the mesoscale. A linear fit to the precipitation rate spatial series is obtained and the ratio of the standard deviation contained in this fit to the standard deviation of the precipitation rate spatial series gives an indication of the fraction of the variability at the largest scales. We find little systematic difference in this ratio as a function of run length. We find that for 88%, 46% and 9% of all runs, the ratio exceeds 0.1, 0.5 and 0.75 respectively. Little difference is found in the distributions for in-cloud and sub-cloud values. This indicates that there is considerable modulation of the precipitation rate on the largest spatial scales observed. A composite power spectrum of precipitation rate is obtained using all the runs in and below cloud is shown in Fig. 13. A Hanning data window was used on each series. Each contributing spectrum was normalised using its variance before compositing. There is much variance between spectra as indicated by the dotted lines that show the 25th and 75th percentiles for each wavenumber range. However, it has still been possible to see that the composite power spectrum follows an approximate power law relation from the smallest scale (2 km) to several tens of km. There are many examples in the literature showing good power law scaling for liquid water path (e.g. Cahalan and Snider 1989) and other cloud variables (e.g. liquid water content, Davis et al. 1996; visible reflectance, Marshak et al. 1997; cloud base height, Wood and Taylor 2001; surface rain rate, Kostinski and Jameson ????) over this same horizontal scale range in marine boundary layer clouds. However, as far as the author is aware, this is the first example of power law scaling in the low precipitation rates found in drizzling boundary layer clouds. Interestingly, the magnitude of the power law exponent here is much lower than those found for liquid water path and content, having a value of -1.16 ($\pm$0.1, 2-σ level). This demonstrates the heightened variability in drizzle at small scales. Again, this scaling is well suited to observation using scanning or vertically-pointing radars.

5. Drizzle timescales

a. Radar reflectivity-precipitation rate relationships

With the increasing use of radars to measure stratocumulus cloud and precipitation properties from both the ground (e.g. Frisch et al. 1995, Yuter and Houze 2000) and from space (e.g. the upcoming Cloudsat mission), there is a need for an understanding of the relationships between parameters measured with the radar and physically significant cloud properties. Precipitation rate is one of the key properties that has great implications for the hydrological cycle and for the dynamics of the boundary layer. It is therefore not surprising that relationships between radar reflectivity and precipitation rate ($Z-R$ relationships) have been most scrutinised, albeit in most cases for clouds with significantly higher precipitation rates than are found in stratocumulus cloud (refs). The measurements presented in this study offer the opportunity of investigating such relationships in stratocumulus cloud.

Before we attempt to look at the $Z - R$ relationships we should first look at the contribution to both radar reflectivity and precipitation rate from drops of different sizes. We need to ascertain whether the microphysical probes that we are using have sufficiently large sample volumes to resolve all the droplet sizes that contribute to the sixth moment of the droplet size distribution, since radar reflectivity Z is defined as

$$Z = 2^6 \int_{r=0}^{\infty} r^6 \frac{dN}{dr} dr \tag{9}$$

with dN/dr here measured in m^{-4} and r in metres. The radar reflectivity has units of m^3. We find that for droplets larger than $r = 60\mu$m, dN/dr is very well modelled using an exponential size distribution in almost all cases (exceptions are discussed later). We therefore fit the observed size distributions at each level for all drops larger than 60 μm using a weighted least-squares fit to give the best-fit exponential. Because of the steep fall off of counted droplets with increasing size and the small sample volume of the 2D-C probe (approximately 0.005 m^3 s^{-1}) hardly any droplets with radii larger than 200 μm were measured on any of the flights. We therefore extrapolate the exponential out to sizes larger than those measured and calculate the contribution to Z and precipitation rate P from droplets 60 μm$< r < \infty$, and compare with the contribution only over the measured range. For the exponential fit we weight each size bin using the inverse square of the Poissonian counting error. Precipitation rate calculated from Eqn. 2 using a single drop terminal velocity relationship calculated from a fourth order polynomial fit to log(w_T), log(r) calculated at $T = 280$ K and $p = 900$ hPa using the full Reynolds number approach set out in Pruppacher and Klett (1997). Tests show that the terminal velocities calculated using the single fitted curve differ by no more than 5% from those calculated using the full theory at all the temperatures and pressures experienced in this study.

Figure 14 shows two examples of the procedure. The size distributions are shown in the upper panels for two cases. The second row shows the size-resolved reflectivity spectra dZ/dr (filled circles) and precipitation rate spectra dP/dz (diamonds). The exponential fits are shown with dotted (dZ/dr) and dashed (dZ/dr) lines, extrapolated to larger sizes. For the case A644 dZ/dr and dP/dr continues to increase beyond the actual measurements, whereas for A764 the peaks in both dZ/dr and dP/dr are well resolved. The lower panels show the cumulative contribution to dBZ (10log$_{10}Z$+180) and P from 60 μm upwards. In the A644 case the extrapolated dBZ is around 7 dBZ higher (a factor of 5 in Z) than that measured with the 2D-C probe and P is more than doubled. For the A764 case there is only a negligible difference between the extrapolated and measured dBZ and P. So, insofar as we can assume the droplets are exponentially distributed, for the A644 case it is likely that droplets larger than those measured may be contributing significantly to the radar reflectivity and precipitation rate whereas in the A764 case this is unlikely.

We present measurements from all in-cloud levels in all flights in Fig. 15, in the form of a comparison of the total dBZ calculated from the extrapolated exponential (60 μm$< r < \infty$, ordinate) and from the 2D-C data (abscissa). The dashed line shows exact agreement and the dotted lines represent the extrapolated exceeding the data by 2.5, 5 and 7.5 dBZ. It is clear that for the majority of flights the differences are small (less than 2.5 in many cases). There is also a tendency for poorer agreement to be found at larger values of dBZ, i.e. for the heavier drizzle cases. We do not include levels below cloud because evaporation of the smaller droplets tends to result in non-exponential size distributions. We did not include flight A641 in this comparison because this flight contained low amounts of drizzle droplets and dN/dr at large drop size was noisy and was not well modelled with an exponential. We do not show the comparison between precipitation rates but the behaviour is similar to that for dBZ. The fractional increase in Z from the data to the exponential extrapolation is a factor of 1.0 to 3.0 times the fractional increase in P. Because the value of this factor is positively correlated with high values of P there are important consequences for the true $Z - P$ relationships in drizzling stratocumulus.

Values of P and Z are derived for the droplet size distribution over the size range $r > 20\mu$m in two ways. The first method is a direct calculation from the measured size distribution giving values P_{data} and Z_{data}. The second uses the exponentially fitted size distribution for $r > 60\mu$m drops and the measured values for $r \leq 60\mu$m, giving values P_{exp} and Z_{exp}. For flight A641 we use only the measured size distribution for reasons mentioned above and so the two methods yield the same values of Z and P. We use least squares fitting to obtain the parameters a and b in the relationship $Z = aP^b$. Table 5 shows the values of a and b for the fits, along with the estimated errors (2-σ level) and the regression coefficient r^2. The most important difference between the relationships is that the exponent b is significantly higher for the extrapolated data ($b = 1.40$) than the measured data ($b = 1.04$). This is a direct result of there being larger fractional increases in Z than in P for the extrapolated distributions compared with the measured ones.

We construct a simple model which generates a $Z - P$ relationship. We assume that an exponential distribution is sufficient to describe the drop size distribution for all $R > 20\mu$m drops. We then make an additional assumption that the terminal velocity of the drops can be described using a single power law $w_T = cr^d$. We find that this power law gives terminal velocities within 20% over the size range $20 < r < 300\mu$m, with the largest errors being at the extremes. We then calculate model P and Z values using equations 2 and 9. Some simple integration over the radius range [0,∞] yields the relationship

$$Z_{model} = \frac{2^6\Gamma(7)}{(4\pi\rho_w c\Gamma(4+d)/3)^{6/(3+d)}} N_{D*}^{1-6/(3+d)} P_{model}^{6/(3+d)} \tag{10}$$

where N_{D*} is the total number of drizzle drops in the exponential size distribution. Because the integration is carried out over the entire $r > 0$ exponential distribution, we are implicitly making the assumption here that drops smaller than $r = 20\mu$m make little difference to the $Z - P$ relationship. The terminal velocity power law approximation has parameters $c = 7.9 \times 10^5$ m$^{-0.52}$ s^{-1} and $d = 1.52$ which is within 20% of the theoretical values in the range $20 < r < 200\mu$m is as large as a factor of 2.5 too high for the smallest drops. However, these small exponentially-distributed drops contribute very little to the precipitation rate for all reasonable exponential distributions and it is concluded that the model is describing drizzle drop populations at least insofar as $Z - P$ relationships are concerned.

Figure 16(a) shows the $Z_{exp} - P_{exp}$ relationship for all in-cloud cases. The value of r^2 for the log-log fit is 0.89. Figure 16(b) shows $Z_{exp}/N_{D*}^{(}1 - 6/(3+d))$ against P_{exp}. Note that $1 - 6/(3+d) = -0.327$. The value of r^2 for the fit is 0.97, significantly better than that for the $Z_{exp} - P_{exp}$ relationship alone. Also shown are the best fit lines (dotted) and the exponential model given in Eqn. 10 (dotted line). There is good agreement between the model and the data, although the model exponent (1.33) is slightly lower than that for the data (1.39 ± 0.04).

These results suggest that, although there is a good correlation between radar reflectivity and precipitation rate, the relationship is not a unique one. Additional information about the drop size distribution is shown to improve the relationship. However, retrievals of precipitation rate from radar reflectivity alone will incur considerable error (Fig. 16(a)), possibly as much as a factor of 3 or 4 in precipitation rate. With additional information, this error can be approximately halved.

6. Parameterisation of cloud microphysical processes

The issue of the processes controlling liquid water content distribution in stratocumulus clouds is currently unresolved. The best hope for making quantitative assessment of the relative roles of entrainment and drizzle is through large eddy simulation (LES). Although LES simulations with fully explicit bin microphysical treatments have been developed (Kogan 1995; Stevens 1996) the computational expense incurred is close to an order of magnitude greater than for equivalent simulations with basic two-mode (cloud water and drizzle water) microphysics (Yefim Kogan, private communication), and so these simulations must currently be run with small domain sizes. With the possibility of mesoscale circulations being important in stratocumulus, and especially its transition to cumulus (Miller and Albrecht 1995; Miller et al. 1998), it would be beneficial to be able to carry out LES with larger domain sizes, provided that accurate representation of microphysical processes can be achieved with two-mode simulations. Khairoutdinov and Kogan (2000), henceforth KK show that this appears to be possible. Using a fully explicit bin microphysical LES, KK derive a parameterisation of autoconversion, accretion and sedimentation processes, that they then apply and compare with the explicit microphysics simulations, with considerable success. Here, we attempt to validate two elements of their scheme: autoconversion and sedimentation. We also compare our observationally-derived process rates with the commonly used schemes of Kessler (1960), Tripoli and Cotton (1980) and Beheng (1994). Autoconversion and accretion rate formulations for these schemes are presented in Table 6. For the Tripoli and Cotton (T+C) scheme we choose a threshold radius of 7 μm for determination of the liquid water content threshold. This is a fairly common choice when applying this scheme in numerical models (refs???).

a. Autoconversion

We calculate autoconversion rates using observed droplet size distributions ($r < 20\mu$m). Collection kernels are as described in part II of this study. Autoconversion rate is estimated by integration of the stochastic collection equation (SCE) in a manner identical to Austin et al. (1995), i.e. by calculating the near-linear rate of drizzle ($r > 20\mu$m) mass increase over 10 minutes of (SCE) integration. This most likely results in more accurate autoconversion rates than the instantaneous method used by Baker (1993). Austin et al. compared their method with the method of Berry and Rheinhardt (1973), which uses the time taken for the mass-weighted mean radius to reach 50 μ, and found differences of around a factor of two (Austin et al. autoconversions being lower). We use size distributions taken from portions of straight and level runs where the liquid water content and droplet concentration were relatively invariant, rather than instantaneous ones. This was necessary because the computational expense of carrying out over 130000 (the approximate total number of seconds of in-cloud data) autoconversion calculations was prohibitive. As a sensitivity test, we found that the mean of the instantaneous autoconversion rates agreed to within a factor of two with our run-mean values.

Figure **??** compares autoconversion rates calculated using the observed data (abscissae) against the parameterised autoconversion rates (ordinates) for the four schemes. There is considerable variation in the rates for the different parameterisations, which is hardly surprising given the differences in dependencies upon cloud liquid water and droplet concentration between schemes (Table 6). The two schemes (Kessler and T+C) which have threshold liquid water contents below which no autoconversion takes place tend to considerably overestimated autoconversion rates when the threshold is exceeded. However the Kessler scheme has a threshold that prohibits any autoconversion at all in many of the cases. The threshold radius used in the Tripoli and Cotton scheme has little physical meaning, and tends to be set to low values so that autoconversion is not entirely prohibited in shallow clouds.

The best agreement between observed and parameterised autoconversion rate is obtained with the Khairoutdinov and Kogan scheme. We did not perform multiple linear regression on our dataset because there was not enough variability in droplet concentration between cases to give robust results. There is, however, enough range in liquid water content values to estimate the power law dependency of autoconversion rate upon cloud liquid water content. Because each flight tended to have little variation in droplet concentration, we used linear regression in logarithmic q_L-autoconversion space on each flight for liquid water content in the range $0.1 < q_L < 1.2$ g m^{-3}, to obtain the exponent α where autoconversion rate$\propto q_L^{\alpha}$. The mean and standard deviation of α were 3.42 and 0.60 respectively. This is higher than the exponents in Kessler (1.0), T+C (2.33) and KK (2.47) but somewhat smaller than that in Beheng (4.7).

We also found that the rate of increase of drizzle droplet concentration N_D due to autoconversion is well modelled with the assumption that newly formed drizzle droplets have a mean volume radius $r_{new} = 22\mu$m, so that the rate can be written as a function of the autoconversion rate

$$\left(\frac{\partial N_D}{\partial t}\right)_{\text{AUTO}} = \frac{3}{4\pi\rho_w r_{new}^3}\left(\frac{\partial q_{L,D}}{\partial t}\right)_{\text{AUTO}}. \tag{11}$$

Our value of r_{new} differs from that in Khairoutdinov and Kogan (2000) who suggest $r_{new} = 25\mu$m, which leads to a 30% smaller rate. However, the value of r_{new} and the drizzle drop concentrations are fairly sensitive to the choice of threshold radius (here 20 μm) and the choice of discrete size bins used in the autoconversion calculations. We find that the value of r_{new} is only slightly larger (by a few percent) than the centre of the smallest radius bin classified as drizzle.

b. Accretion

Accretion rates were derived in the same manner as autoconversion rates by integration of the SCE except that the full droplet size distribution was used. The rate of drizzle droplet mass increase thus obtained is that due to the combined effects of autoconversion and accretion, and so we calculate the latter by subtraction of the derived autoconversion rate from the combined rate.

Accretion rates are compared in Fig. **??**. The parameterisation schemes all perform better than for autoconversion rate, with T+C being the least biased. Biases in the other schemes do not exceed 70%, which is encouraging. For reasons mentioned above the autoconversion rates (and also accretion rates) are likely to be accurate to no better than a factor of two. The formulations for accretion rate all have similar dependencies upon cloud and drizzle liquid water content.

The rate of loss of cloud droplets is parameterized in Khairoutdinov and Kogan (2000) by assuming that all collected drops (through both autoconversion and accretion) have a size equal to the mean volume radius of the cloud droplets. We test that by comparison with the rate of cloud droplet loss using the SCE integrations. Figure 19(a) shows the rates derived from the observed drop size distributions against the parameterization. For observed droplet loss rates higher than around 100 m^{-3} s^{-1} the rates in most cases agree to within a factor of two. For lower loss rates the parameterization tends to overestimate the rate of droplet loss. However, a droplet loss rate of 100 m^{-3} s^{-1} means that in one hour only 0.36 cloud droplets are lost to autoconversion/accretion which is rather insignificant.

We also compare our cloud droplet loss rates with those from Beheng (1994) which has separate rates for the loss due to autoconversion, accretion and self-collection of cloud droplets. Note that the method we use to determine the droplet loss rates by solving the SCE includes self-collection (i.e. where two cloud droplets coalesce but form another cloud droplet) in the autoconversion drop loss calculation. We compare the total drop loss due to both autoconversion and accretion in Fig. 19(b) for the Beheng (1994) parameterization. As with K+K, the rates compare favourably for the larger rates, and there is a tendency for overprediction especially at the smaller rates. Neither Tripoli and Cotton (1980) or Kessler (1960) include terms to account for removal of cloud droplets due to the coalescence mechanism.

c. Sedimentation

Parameterization of the drizzle process requires expressions for the rate at which the droplet population sediments. Given that the drizzle droplet population is well modelled using an exponential distribution, parameterization of drizzle drop sedimentation rates will require specification of the rate at which both the drop number and a second moment of the distribution falls. It is a simple matter to calculate the theoretical number and mass fall rates from knowledge using the exponential framework. The mass fall rate is simply the precipitation rate defined in Eqn. 2, and the number fall rate is

$$P_{number} = \int_0^\infty w_T \frac{dN}{dr} dr. \quad (12)$$

The vertical advection equation for number concentration can then be solved to yield changes to the drizzle drop concentration at each level due to sedimentation. For the exponential distribution, the precipitation rate P and number fall rate P_{number} can be written as

$$P = \frac{4\pi\rho_w}{3} N_{D*}\Gamma(4+d)\overline{r*}^{3+d} \quad (13)$$

$$P_{number} = cN_{D*}\Gamma(1+d)\overline{r*}^{d} \quad (14)$$

using the same power law relationship for the terminal velocity as presented in Section ????. Typically, P and P_{number} are expressed as functions of drizzle liquid water content $q_{L,D*} \equiv 8\pi\rho_w N_{D*}\overline{r}^3$ and drizzle drop concentration.

$$P = \frac{4\pi\rho_w c\Gamma(4+d)}{(4\pi\rho_w\Gamma(4)/3)^{1+d/3}} q_{L,D*}^{1+d/3} N_{D*}^{-d/3} \quad (15)$$

$$P_{number} = \frac{c\Gamma(1+d)}{(4\pi\rho_w\Gamma(4)/3)^{d/3}} q_{L,D*}^{d/3} N_{D*}^{1-d/3} \quad (16)$$

We plot the mass and number fall rates P and P_{number} divided by $N_D^{-d/3}$ and $N_D^{1-d/3}$ respectively against the drizzle water content $q_{L,D}$ in Fig. 20(a,b). There is reasonably good agreement (certainly in the gradient) between the observations and the exponential model even though we have used parameters derived from only the $r > 20\mu$m drops. This fact is the likely cause of the small offsets between observations and the exponential model. We have also plotted the mass and number fall speeds as parameterized using Khairoutdinov and Kogan (2000) against the observed ones in Fig. 20(c,d). In most cases these agree to within a factor of two. Note that in all cases, the observed fall rates include the contribution from the exponential extrapolaion at *large* sizes. The regression coefficients r^2 for the mass fall rates is 0.97 (exponential) and 0.96 (K+K); for the number fall rates r^2 is equal to 0.86 (exponential) and 0.96 (K+K). The K+K precipitation rates are generally slightly lower and the number rates slightly higher than those from the observations. The cause of these differences is not clear but may represent differences in the drop terminal velocity relationships used in both cases.

Table 1: Flight numbers, dates, locations, times, cloud type, mean heights of cloud base $\overline{z_{CB}}$ and cloud top ($\overline{z_i}$), mean liquid water path $\overline{LWP}$ ($\pm$ error), mean in-cloud droplet concentration N_* and mean cloud base precipitation rate P_{CB}. Note that the errors are errors in the mean value rather and not estimates of the variability in that parameter.

Flight	Date	Location	Time [local]	Type	$\overline{z_{CB}}$ [m]	$\overline{z_i}$ [m]	$\overline{LWP}$ [g m^{-2}]	N_* [cm^{-3}]	P_{CB} [mm d^{-1}]
A049	6 Dec 90	SW App.	12-15	Sc	825±23	1450±34	260±44	310	0.49
A209	12 Jun 92	Azores	00-04	Sc	310±44	705±27	170±34	120	0.47
A439	29 Feb 96	NW Ireland	12-15	Sc	780±19	1150±9	100±15	90	0.24
A641	3 Dec 98	S. North Sea	11-16	Sc	430±7	1110±14	360±16	420	0.054
A644	14 Dec 98	SW App.	12-15	St	150±75	1800[1]	90±50	20	0.66
A648	28 Jan 99	SW App.	12-15	St	190±18	1550[1]	85±50	8	1.12
A649	29 Jan 99	SW App.	12-16	Sc	450±9	775±13	80±6	60	0.095
A693	8 Jul 99	NW Ireland	12-16	St/Sc	115±21	395±3	80±3	110	0.41
A762	12 Jun 00	SW App.	12-16	St/Sc	180±13	495±11	80±5	95	0.28
A763	14 Jun 00	SW App.	12-16	St/Sc	245±18	485±14	45±2	85	0.34
A764	15 Jun 00	SW App.	12-16	St/Sc	≈20[2]	320±6	70±6	65	0.44
A767	28 Jun 00	North Sea	12-15	Sc w/Cu	935±24	1350±10	90±10	110	0.78

Notes: 1. The cloud consisted of two or more layers which were heterogeneous and often had indistinct vertical boundaries. The figure for mean cloud top given is for the uppermost layer. 2. The aircraft was not able to descend to cloud base due to visibility restrictions. This cloud base was estimated by extrapolation of the profiles of liquid water content from higher levels.

Figure captions

Figure 1. Profiles of (a) temperature; (b) total water content; (c) liquid water content (line) and cloud fraction (circles); (d) droplet concentration for flight A644. In (a), (b) and (c) circles represent run means from 60 km horizontal runs.

Table 2: Values of mean in-cloud total water content q_*, cloud base pressure p_{CB}, temperature T_{CB} and ratio of observed to adiabatic liquid water path f_{ad}. The error in f_{ad}, given at the 1-σ level, is estimated using a simple model of cloud structure (see text).

Case	q_*	p_{CB}	T_{CB}	f_{ad}
	[g kg^{-1}]	[hPa]	[K]	
A049	5.1	928	275.5	0.60 ± 0.10
A209	10.1	987	287.3	0.92 ± 0.18
A439	4.6	940	273.9	0.77 ± 0.08
A641	3.1	960	270.7	0.99 ± 0.04
A644	8.4	996	285.1	0.08 ± 0.09
A648	6.6	993	282.0	0.14 ± 0.08
A649	6.6	972	279.7	0.72 ± 0.05
A693	9.6	1005	286.0	0.77 ± 0.03
A762	9.4	998	286.0	0.67 ± 0.04
A763	9.2	993	285.7	0.67 ± 0.02
A764	8.9	1011	285.0	0.59 ± 0.05
A767	4.8	909	274.6	0.64 ± 0.07

Table 3: Thermodynamic and dynamic details of the cases studied. From left to right: sea surface temperature SST; 10 metre wind speed U_{10}; friction velocity u_*; mean in-cloud value of the vertical wind speed standard deviation $\overline{\sigma_w}$; mean in-cloud vertical wind integral scale $\overline{\lambda_w}$; ratio of inversion height to the Monin Obukhov length -z_i/L_{MO}; mean inversion jump in virtual potential temperature $\Delta\theta_v$; mean inversion jump in total water content Δq_T.

Case	SST	U_{10}	u_*	w_*	$\overline{\sigma_w}$	$\overline{\lambda_w}$	-z_i/L_{MO}	$\Delta\theta_v$	Δq_T
	[K]	[m s^{-1}]	[m s^{-1}]	[m s^{-1}]	[m s^{-1}]	[m]	[m]	[K]	[g kg^{-1}]
A049	283.3	5.1	0.19	0.63	0.58	175	14.6	5.7	-2.0
A209	290.3	8.1	0.26		0.70	150		2.9	-1.0
A439	281.6	6.2	0.25	0.89	0.59	130	18.0	5.5	-3.6
A641	282.5	0.7	0.13	0.97	0.65	230	166	4.3	-0.5
A644	284.7	9.7	0.47	-	0.37	200	-0.50	n/a[1]	n/a[1]
A648	283.9	13.3	0.37	0.33	0.25	200	0.28	n/a[1]	n/a[1]
A649	283.6	2.2	0.14	0.62	0.28	180	34.8	2.7	-1.1
A693	286.4	10.7	0.34	0.43	0.38	35	0.81	5.4	-0.8
A762	286.5	11.3	0.40	-	0.30	60	-0.27	4.4	-0.9
A763	287.2	7.3	0.18	-	0.26	160	-0.84	4.8	-0.3
A764	287.7	1.3	0.14	0.44	0.28	80	12.4	2.3	-0.5
A767	285.1	10.1	0.38	0.95	0.50	130	6.25	3.6	-2.7

[1] These cases contained multiple weak inversions ($\Delta\theta_v < 1$ K; $\Delta q_T < 0.5$ g kg^{-1}) both in and above the cloud layers and it is therefore not possible to define a good measure of the inversion jumps.

Table 4: In-cloud mean drizzle drop concentration $\overline{N_{d,D}}$, liquid water content $\overline{q_{L,D}}$ and precipitation rate $\overline{P}$. Also given are cloud top ($0.8 < z_* < 1.0$) and cloud base ($0.0 < z_* < 0.2$) values of the drizzle drop volume radius $r_{v,D}$

Case	$\overline{N_{d,D}}$ [l^{-1}]	$\overline{q_{L,D}}$ [10^{-3} g m^{-3}]	$\overline{P}$ [mm day^{-1}]	$r_{v,D}$ (base) [μm]	$r_{v,D}$ (top) [μm]
A049	37	11.3	0.51	53	38
A209	60	11.2	0.39	46	29
A439	30	7.5	0.26	45	35
A641	18	2.2	0.08	31	29
A644	59	20.9	0.99	42	43
A648	147	30.9	0.80	53	32
A649	46	6.8	0.17	38	30
A693	135	17.6	0.32	37	28
A762	170	17.7	0.28	36	26
A763	118	15.3	0.27	39	27
A764	89	21.8	0.58	44	35
A767	141	21.0	0.67	53	25

Table 5: Details of the $Z - P$ relationships derived from the measured and extrapolated size distributions. Numbers in parentheses indicate 2-σ errors in a and b (percentage for a, absolute for b).

Relationship	a	b	r^2
$Z_{data} = aP_{data}^b$	2.2×10^{-19}	1.04	0.89
	[12.6%]	[0.07]	
$Z_{exp} = aP_{exp}^b$	3.89×10^{-19}	1.40	0.92
	[16.0%]	[0.08]	
$Z_{data} = aN_{D*}^{-0.327}P_{data}^b$	1.33×10^{-17}	1.18	0.92
	[11.4%]	[0.07]	
$Z_{exp} = aN_{D*}^{-0.327}P_{exp}^b$	1.95×10^{-17}	1.39	0.97
	[8.6%]	[0.04]	
$Z_{model} = aN_{D*}^{-0.327}P_{exp}^b$	1.44×10^{-17}	1.33	n/a

Table 6: Autoconversion and accretion formulations for the four parameterisations validated. Units are kg m^{-3} for liquid water contents and m^{-3} for droplet concentrations. The air density ρ is expressed in units of kg m^{-3}. $H(x)$ is the Heaviside step function.

Scheme	Autoconversion rate [kg m^{-3} s^{-1}]	Accretion rate [kg m^{-3} s^{-1}]
Khairoutdinov and Kogan (2000)	$Aq_L^{2.47}N_d^{-1.79}\rho^{-1.47}$ ($A = 7.42 \times 10^{13}$)	$67(q_Lq_D)^{1.15}\rho^{-1.3}$
Kessler (1960)	B max($q_L - q_{L,0}$,0) ($B = 1.0d-3$; $q_{L,0} = 5 \times 10^{-4}$)	$0.29 q_L q_D^{7/8} N_d^{1/8}$
Beheng (1994)	$Cd^{-1.7}q_L^{4.7}N_d^{-3.3}$ ($C = 4.8 \times 10^{14}$; $d = 9.9$ for $N_d < 200$ cm^{-3} $d = 3.9$ for $N_d > 200$ cm^{-3})	$6.0 q_L q_D$
Tripoli and Cotton (1980)	$Dq_L^{7/3}N_d^{-1/3}H(q_L - q_{L,0})$ ($D = 3268$, assumes E_C=0.55 $q_{L,0}$ assumes $r_{cm} = 7\mu$m)	$4.7 q_L q_D$

7. References

Austin, P., Wang, Y., Pincus, R. and Kujala, V., 1995a. Precipitation in stratocumulus clouds: observations and modelling results. *J. Atmos. Sci.*, **52**, 2329-2352.

Austin, P, Siems, S. and Wang, Y., 1995b. Constraints on droplet growth in radiatively cooled stratocumulus clouds. *J. Geophys. Res.*, **100**, D7, 14231–14242.

Berry E. X. and Reinhardt, R. L., 1974. An analysis of cloud droplet growth by collection. Part I: Double distributions. *J. Atmos. Sci.*, **31**, 1814-1824.

Bott, A., 1989. A positive definite advection scheme obtained by nonlinear renormalization of the advective fluxes. *Mon. Wea. Rev.*, **117**, 1006-2636.

Bott, A., 1998. A flux method for the numerical solution of the stochastic collection equation. *J. Atmos. Sci.*, **55**, 2284-2293.

Bretherton, C. S., Austin, P. and Siems, S. T., 1995. Cloudiness and marine boundary layer dynamics in the ASTEX Lagrangian Experiments. Part II: Cloudiness, drizzle, surface fluxes and entrainment. *J. Atmos. Sci.*, **52**, 2724-2735.

Cooper, W. A., 1989. Effects of variable growth histories on droplet size distributions. Part I: Theory. *J. Atmos. Sci.*, **46**, 1301–1311.

Davis, M. H., 1972. Collisions of small droplets: Gas kinetic effects. *J. Atmos. Sci.*, **29**, 911-915.

Edwards, J. M. and Slingo, A., 1996. Studies with a flexible new radiation code. I: Choosing a configuration for a large-scale model. *Quart. J. Roy. Meteorol. Soc.*, **122**, 689–720.

Feingold, G., Cotton, W. R., Kreidenweis, S. M. and Davis, J. T., 1999. The impact of giant cloud condensation nuclei on drizzle formation in stratocumulus: implications for cloud radiative properties. *J. Atmos. Sci.*, **56**, 4100-4117.

Golovin, A. M., 1963. The solution of the coagulation equation fro cloud droplets in a rising air current. *Izv. Akad. Nauk. SSSR. Ser. Geofiz.*, **5**, 783-791.

Gong, S. L. and Barrie, L. A., 1997. Modeling sea-salt aerosols in the atmosphere. 1: Model development.

J. Geophys. Res., **102**, 3805-3818.

Hall, W. D., 1980. A detailed microphysical model within a two-dimensional dynamic framework: Model description and preliminary results. *J. Atmos. Sci.*, **37**, 2486-2507.

Hunt, J. C. R., 1981. Diffusion in the SBL. *Atmospheric turbulence and air pollution modelling: A course held in the Hague*, 21-25 September 1981, F. Nieuwstadt and H. van Dop, Eds, D Reidel, 231-274.

Jonas, P. R., 1972. The collision efficiency of small drops. *Quart. J. Roy. Meteorol. Soc.*, **98**, 681-683.

Khairoutdinov and Kogan
Korolev, A. V., Strapp, J. W. and Isaac, G. A., 1998. Evaluation of the accuracy of PMS Optical Array probes. *J. Atmos. Oceanic Technol.*, **15**, 708-720.

Laird, N. F., Ochs III, H. T., Rauber, R. M. and Jay Miller, L., 1998 Microphysical properties of Florida small cumulus clouds. Part I: Observations. *Proceedings of AMS Conference on Cloud Physics*, 486-489, 17-21 August 1998, Everett, USA.

Monahan E. C., Spiel, D. E. and Davidson, K. L., 1986 A model of marine aerosol generation via whitecaps and wave disruption. In *Oceanic Whitecaps*, edited by E. C. Monahan and G. Mac Niocaill, 167-174, D. Riedel, Norwell, Mass., USA

Nicholls, S. and Leighton, J., 1986 An observational study of the structure of stratiform cloud sheets: Part 1. Structure. *Quart. J. Roy. Meteorol. Soc.*, **112), 431–460.**

Nicholls, S., 1987. A model of drizzle growth in warm, turbulent, stratiform clouds. *Quart. J. Roy. Meteorol. Soc.*, 113, 1141-1170.

O'Dowd, C. D. and Smith, M. H., 1993. Physicochemical properties of aerosol over the Northeast Atlantic: Eivdence for wind-speed-related submicron sea-salt aerosol production. *J. Geophys. Res.*, 98, 1137-1149.

Politovich, M. K. and Cooper, W. A., 1988. Variability of the supersaturation in cumulus clouds. *J. Atmos. Sci.*, 45, 1651–1664.

Rogers, R. R. and Yau, M. K., 1989. *A short course in cloud physics.* **Third edition, Pergamon Press, Oxford, UK.**

Rogers, D. P., Johnson, D. W. and Friehe, C. A., 1995. The stable internal boundary layer over a coastal sea. Part I: Airborne measurements of the mean and turbulence structure. *J. Atmos. Sci.*, 52, 667-683.

Stevens, B., Feingold, G., Cotton, W. R. and Walko, R. L., 1998. Elements of the microphysical structure of numerically simulated nonprecipitating stratocumulus. *J. Atmos. Sci.*, 53, 980–1006.

Stull, R. B., 1984. Transilient turbulence theory. Part I: The concept of eddy-mixing across finite distances. *J. Atmos. Sci.*, 41, 3351-3367.

Stull, R. B. and Hasegawa, T., 1984. Transilient turbulence theory. Part II: Turbulent adjustment. *J. Atmos. Sci.*, 41, 3368-3379.

Stull, R. B., 1988. *An introduction to boundary layer meteorology.* **Kluwer Academic Publishers, Dordrecht, The Netherlands.**

Wood, R., 2000. Parametrization of the effect of drizzle upon the droplet effective radius in stratocumulus clouds. *Quart. J. Roy. Meteorol. Soc.*, 126, 3309–3324.

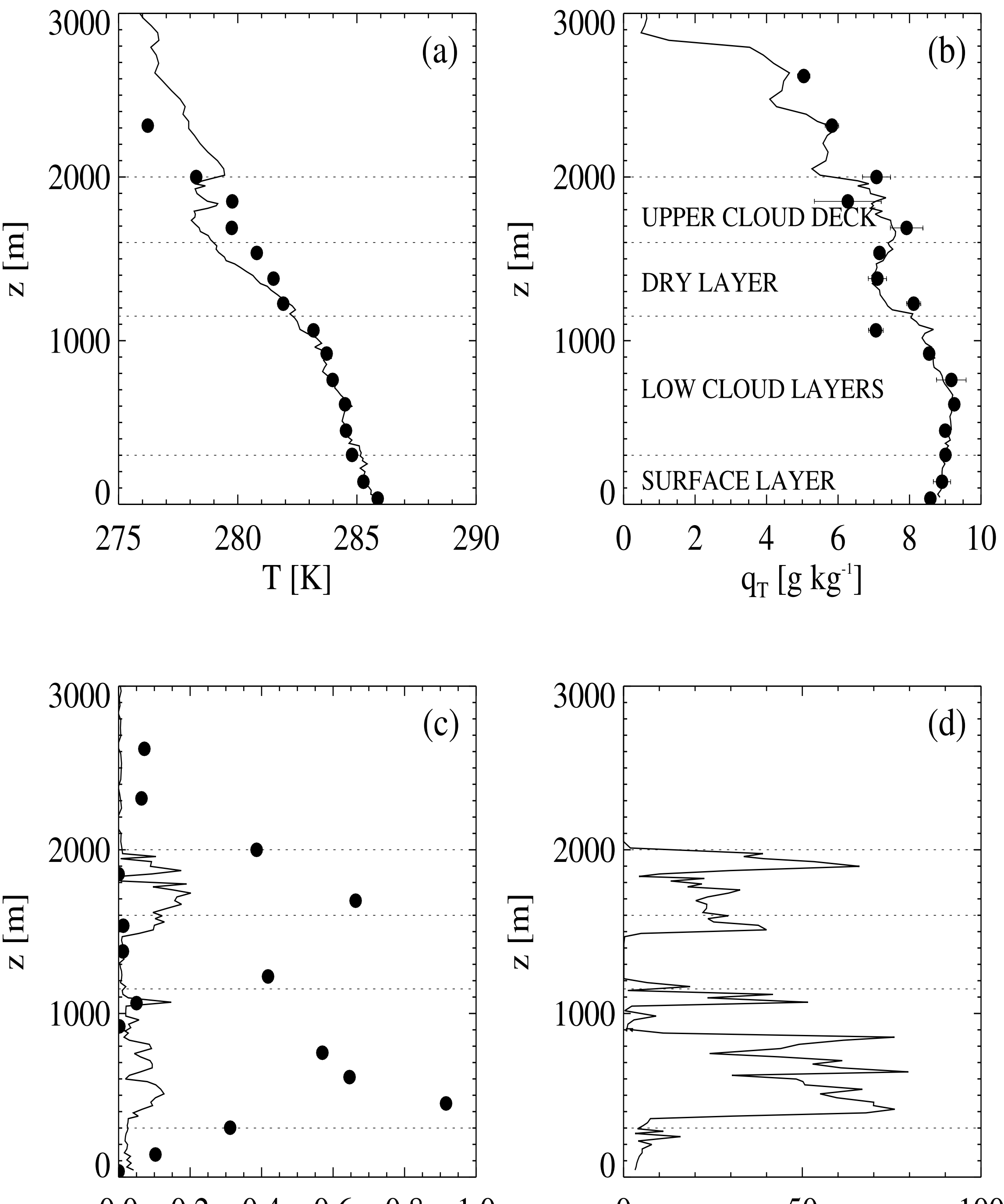
(a)
(b)
(c)
(d)
3000
2000
1000
0
z [m]
275
280
285
290
T [K]
0
2
4
6
8
10
q_T [g kg^{-1}]
UPPER CLOUD DECK
DRY LAYER
LOW CLOUD LAYERS
SURFACE LAYER
0.0
0.2
0.4
0.6
0.8
1.0
q_L [g kg^{-1}], CF (circles)
0
50
100
N_d [cm^{-3}]

Figure 1:

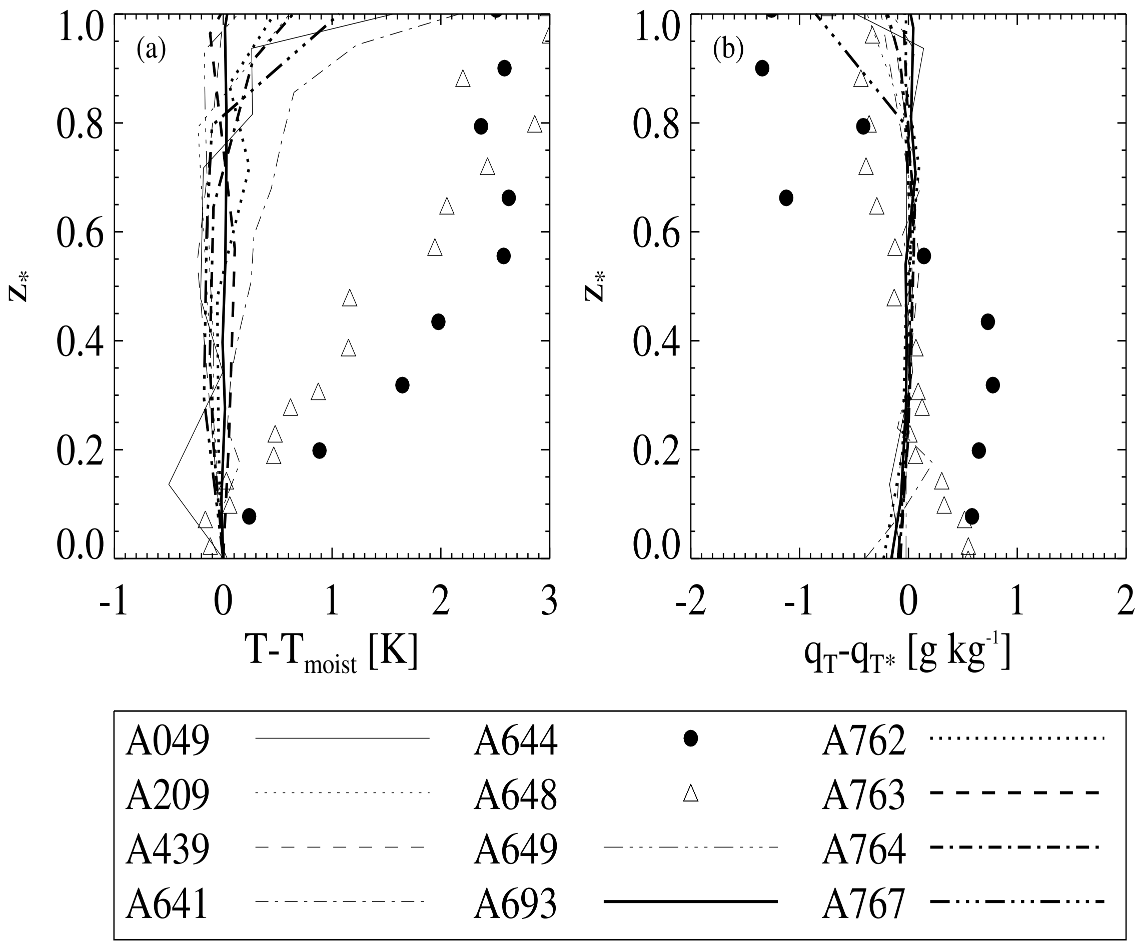

Figure 2: (a) Temperature and (b) total water content in-cloud profiles for each of the cases. Symbols are For (a) the difference between the observed mean temperature at each height and the moist adiabatic temperature is plotted as a function of normalised height. For (b) the difference between the mean total water content at each height and the mean total water content averaged over the entire cloud layer is plotted. The same linestyles and symbols are used throughout this article whenever data from multiple flights are plotted on the same axes.

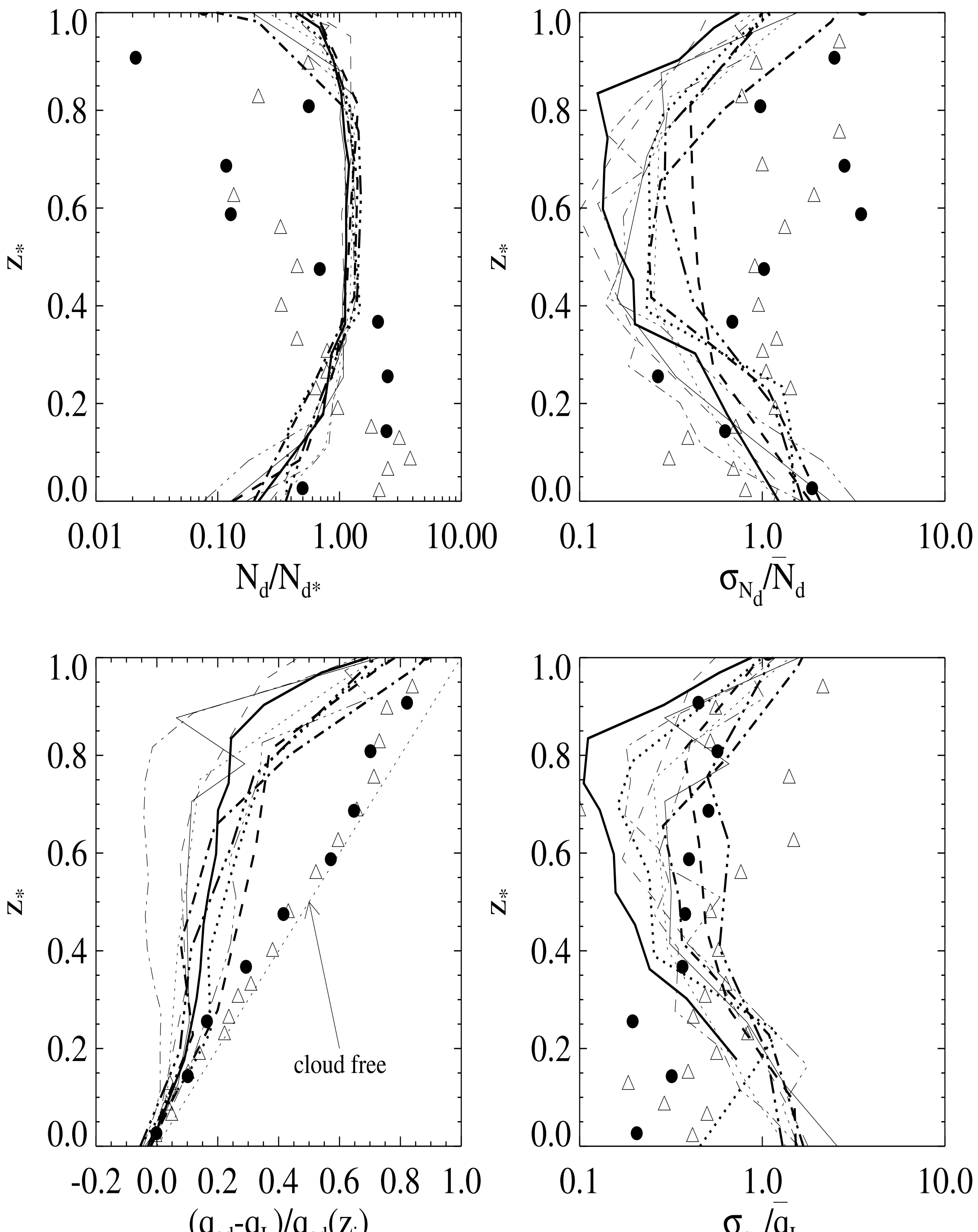

Figure 3: Profiles of (a) droplet concentration N_d, (b) standard deviation of droplet concentration at each level normalised with the mean at each level; (c) values of the subadiabaticity parameter $(q_{ad} - q_L)/q_{ad}(z_i)$ for which zero represents a perfectly adiabatic cloud. The dotted line represents cloud free conditions; (d) the standard deviation of the liquid water content normalised with the mean at that level. Symbolia are the same as for Fig. 2.

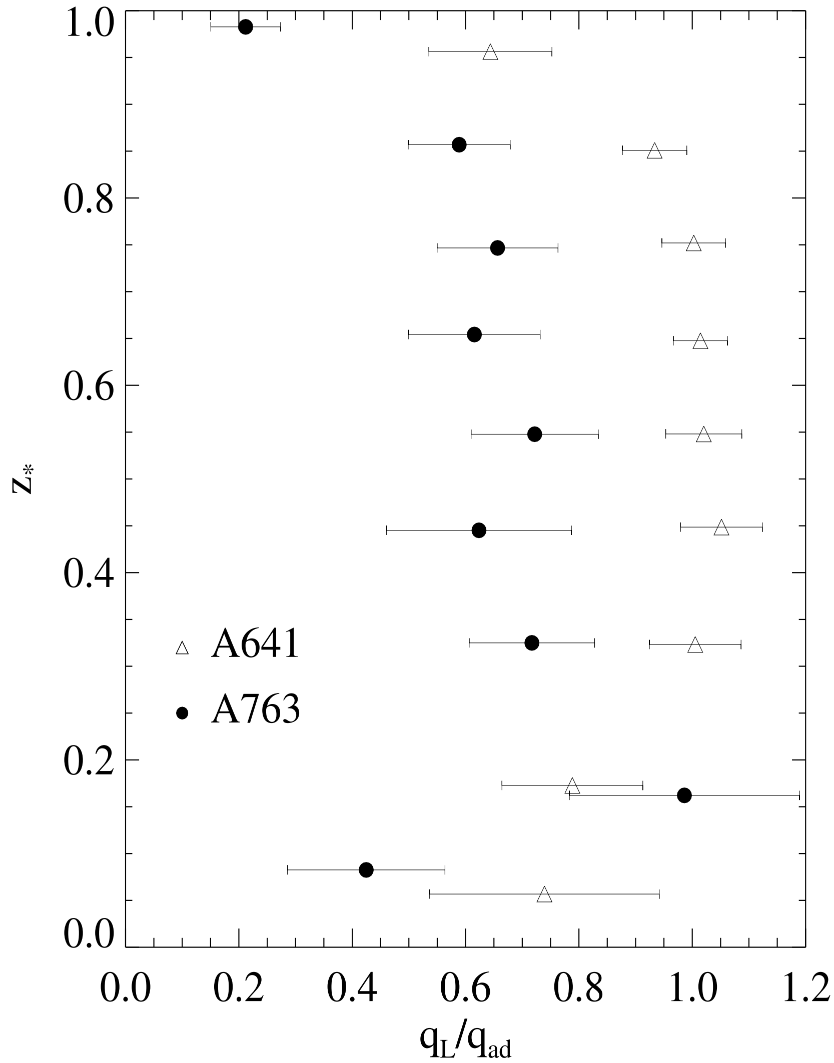

Figure 4: The mean ratio of liquid water content to adiabatic liquid water content (adiabaticity ratio) as a function of height in cases A763 (filled circles) and A641 (triangles), using the individual profile method (see text). These clearly show that the adiabaticity ratio is roughly constant through the bulk of the cloud ($0.2 < z_* < 0.9$). The error bars show the error in the mean (95% confidence level) derived only from the spread in the data values from different profiles. The estimated errors in q_L/q_{ad} derived from a simple model of the cloud structure are ± 0.09 and ± 0.07 (95% level) for A641 and A763 respectively which do not differ markedly from the errors derived from the spread in data.

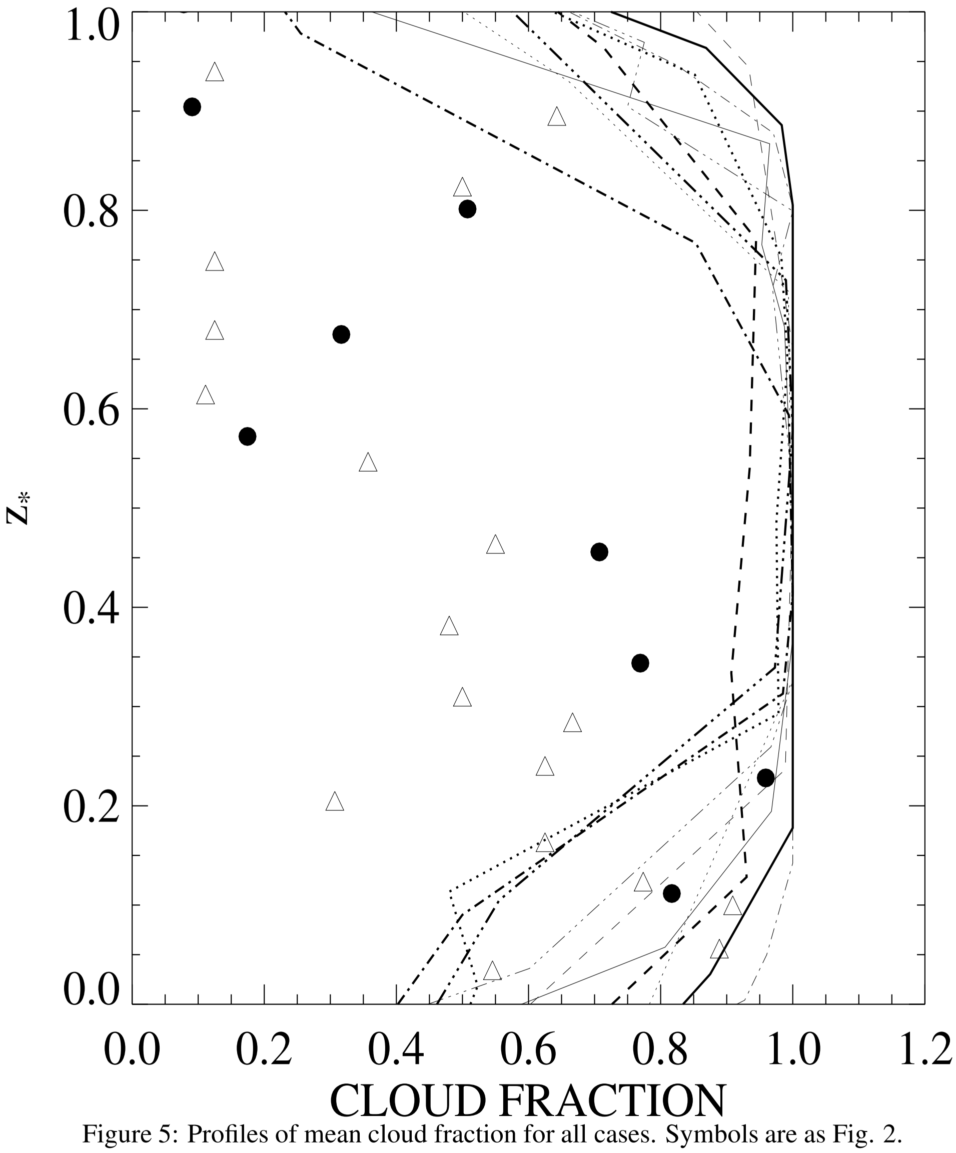

Figure 5: Profiles of mean cloud fraction for all cases. Symbols are as Fig. 2.

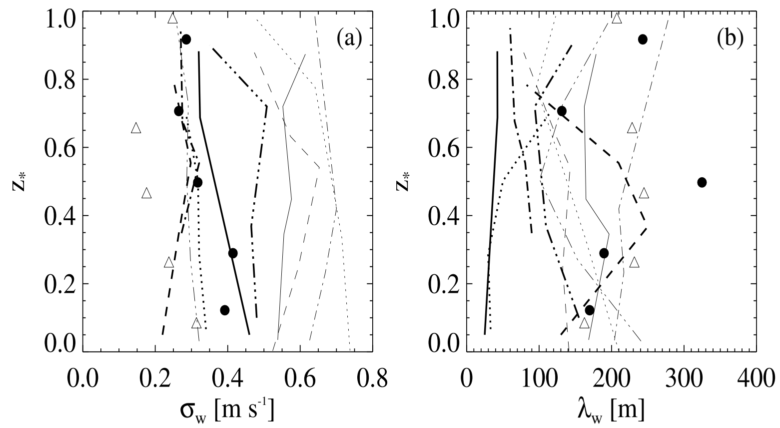

Figure 6: Profiles of vertical wind standard deviation for all cases. Symbols are as Fig. 2.

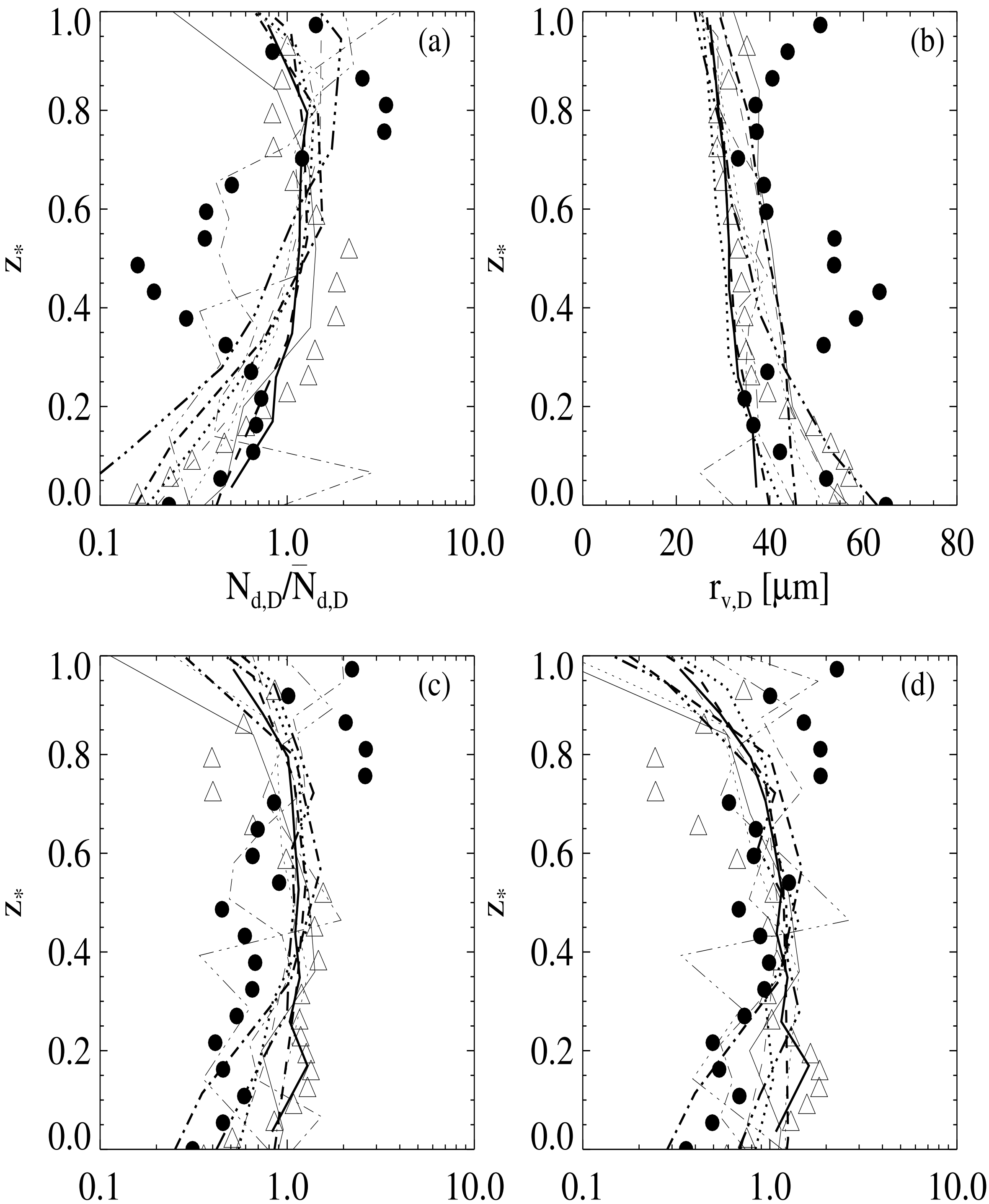

Figure 7: Profiles of characteristics relating to the drizzle drops, which are defined here as drops with radii larger than 20 μm. (a) Drizzle droplet concentration $N_{d,D}$ normalised with the mean drizzle droplet concentration in the cloud layer; (b) volume radius of drizzle drops $r_{v,D}$ which increases towards cloud base; (c) liquid water content contained in the drizzle drops normalised with the mean value for the cloud layer; (d) precipitation rate normalised with the mean value in the cloud layer. Symbols are as Fig. 2.

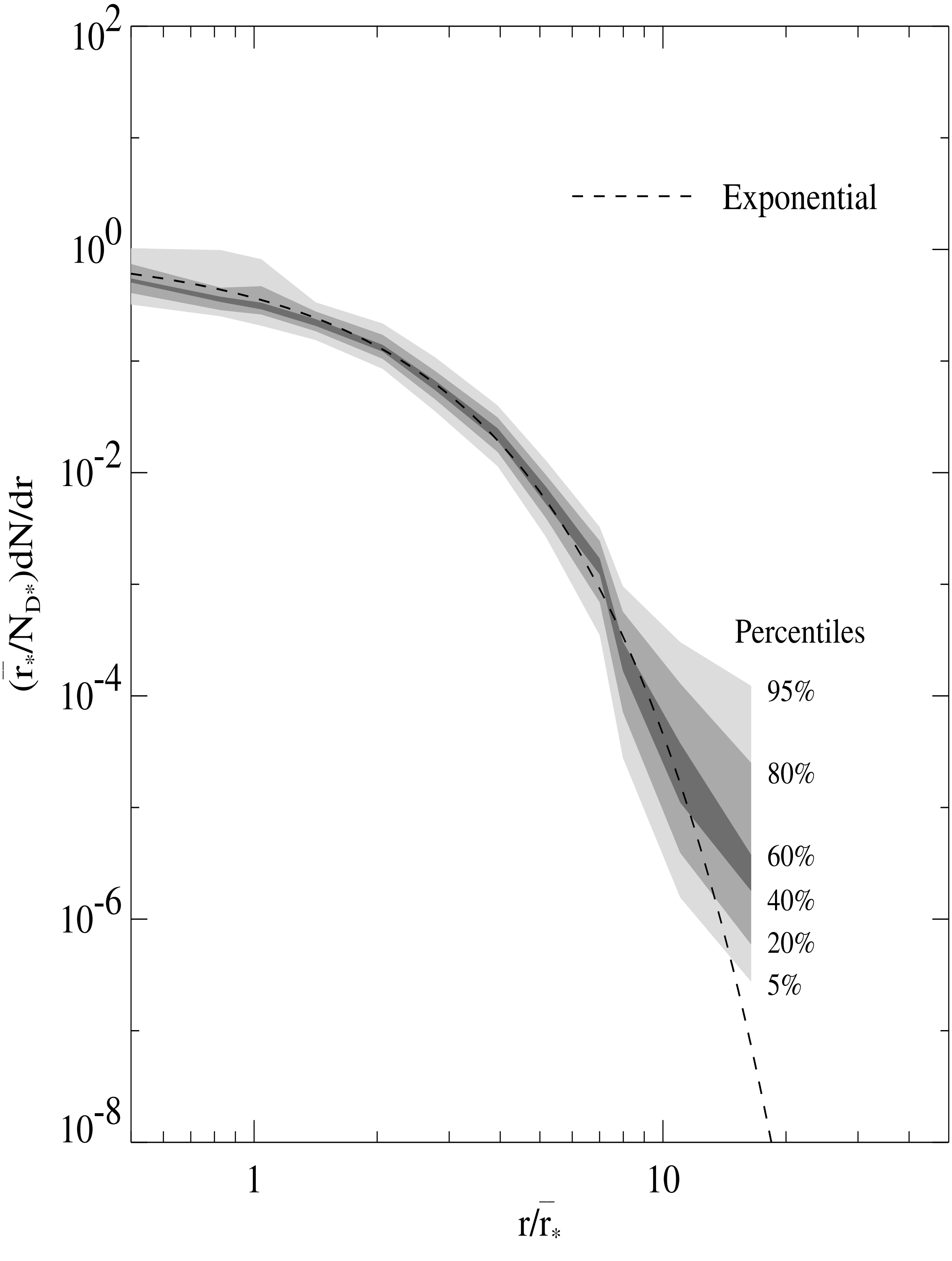

Figure 8: Normalised droplet spectra $(\overline{r_*}/N_{D*})dN/dr$ at all in-cloud levels (103 spectra) plotted against $r/\overline{r_*}$. The universal exponential distribution $(\overline{r_*}/N_{D*})dN/dr = \exp(-r/\overline{r_*})$ is shown by the dashed line. The spectra are shown by the contours which denote percentiles of all the distributions in each $r/\overline{r_*}$ class. The lightest colored contour therefore contains 95% of all the size distributions in each class.

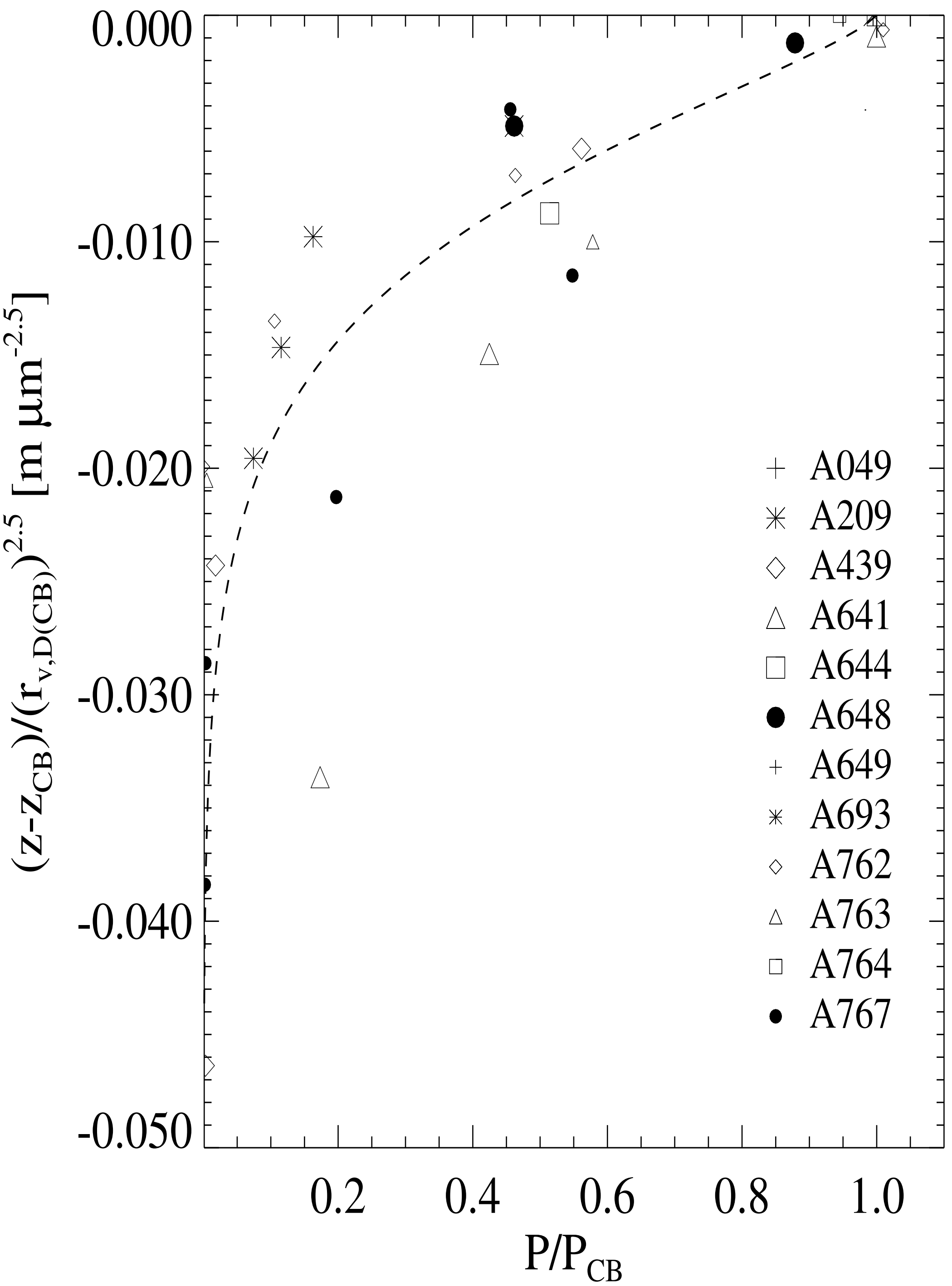

Figure 9: Sub-cloud precipitation rates normalised with cloud base values plotted as a function of height below cloud base normalised with the $r > 20\mu$m mean volume radius of the size distribution at cloud base taken from Table 4. The shaded region shows the range for the simple sedimentation evaporation model. The dashed line represents a reasonable fit to the observations.

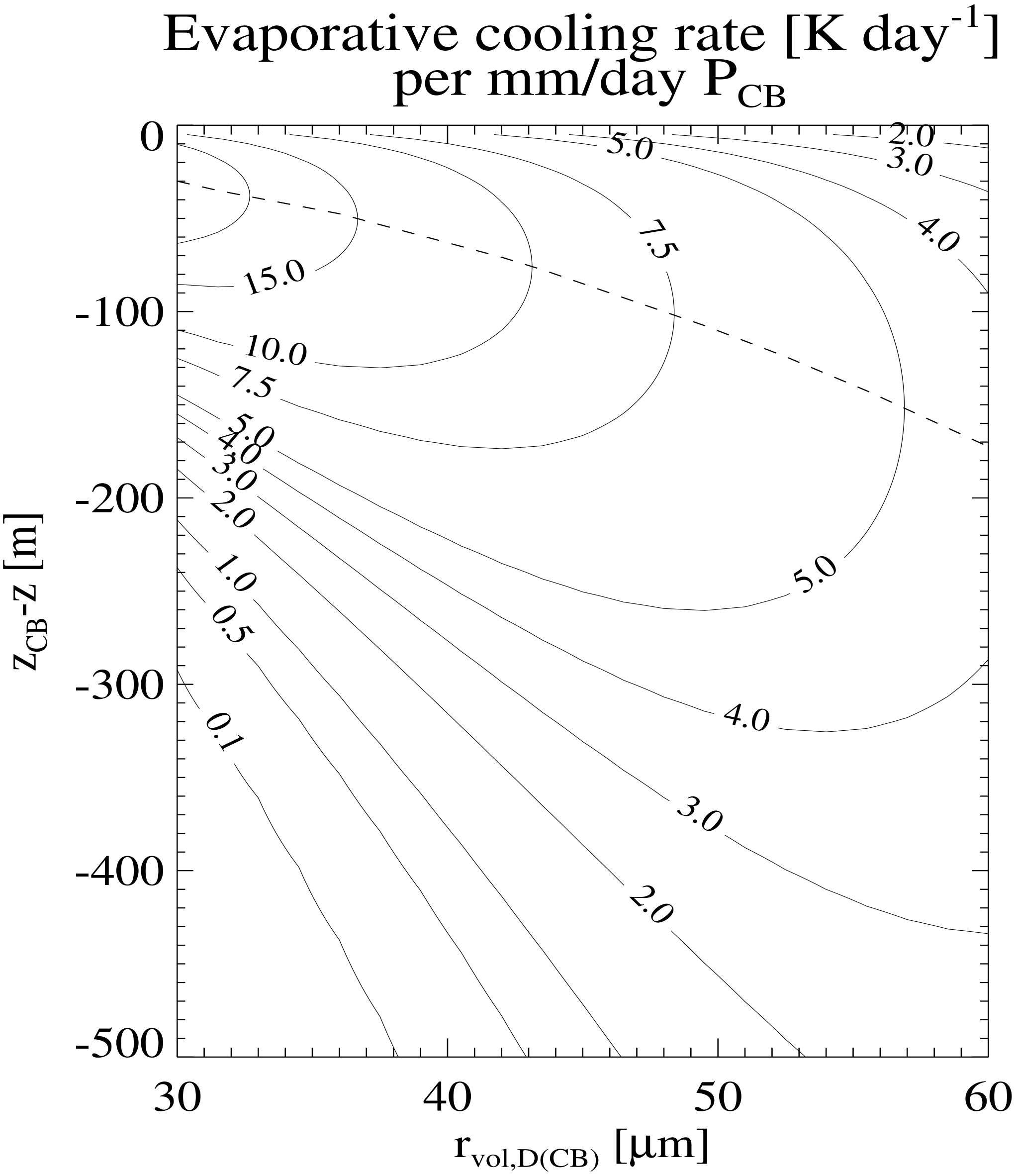

Figure 10: Sedimentation-evaporation model cooling rates for the evaporation of drizzle below cloud base as a function of height below cloud base and mean volume radius of the drizzle drops at cloud base. The cooling rates are expressed in K day^{-1} per mm day^{-1} of cloud base precipitation rate. A dry adiabatic layer is assumed below cloud base. The dashed line shows the level of the peak cooling rate.

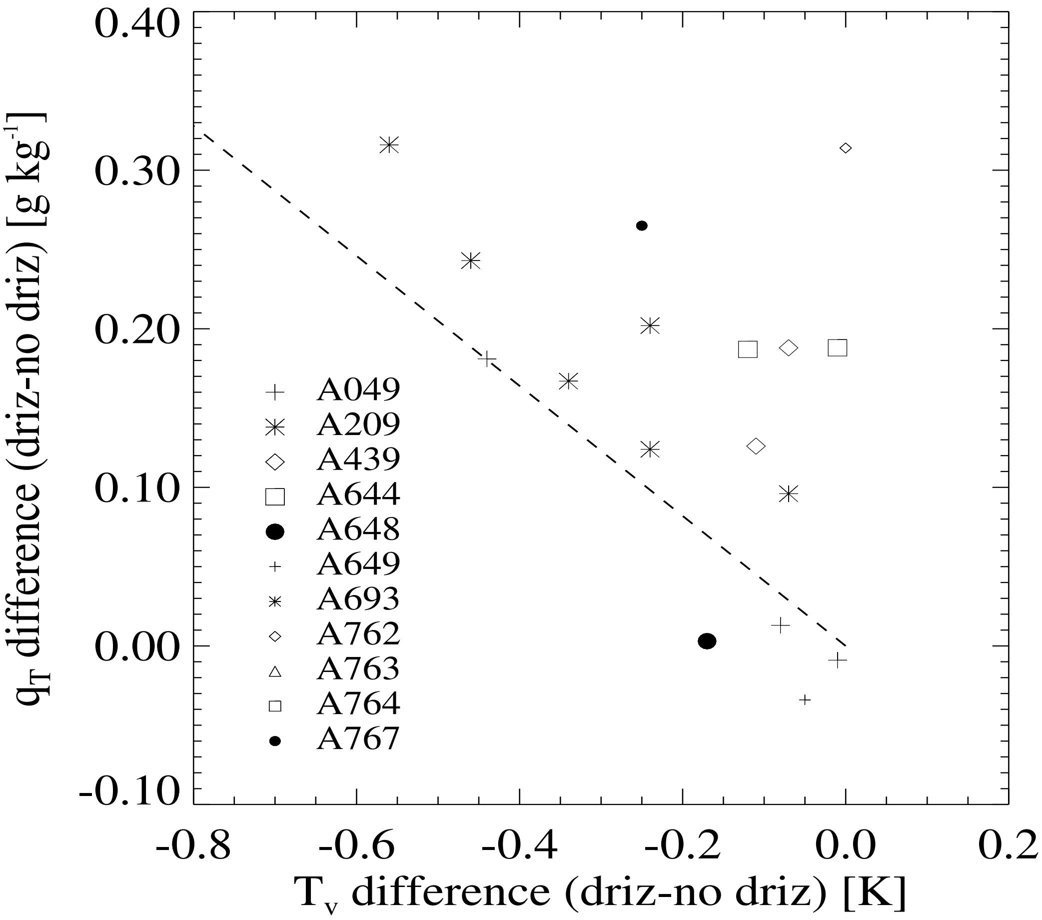

Figure 11: Difference between the mean subcloud virtual temperature (T_v, abscissa) and mean specific humidity (q_v, ordinate) in drizzle regions and drizzle-free regions for suitable subcloud runs. The dashed line corresponds to differences caused purely by evaporation.

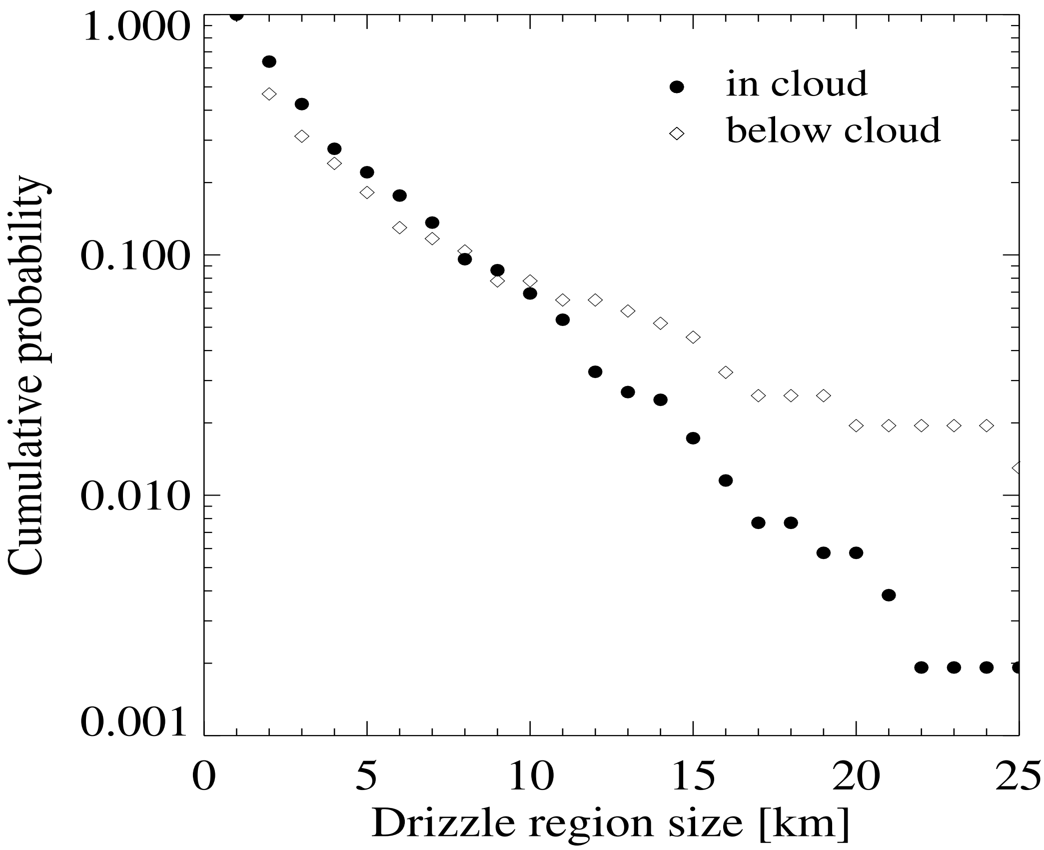

Figure 12: Cumulative distribution of drizzle cell sizes from all flights for in-cloud and below cloud runs. The ordinate shows the fraction of regions with sizes larger than shown on the abscissa.

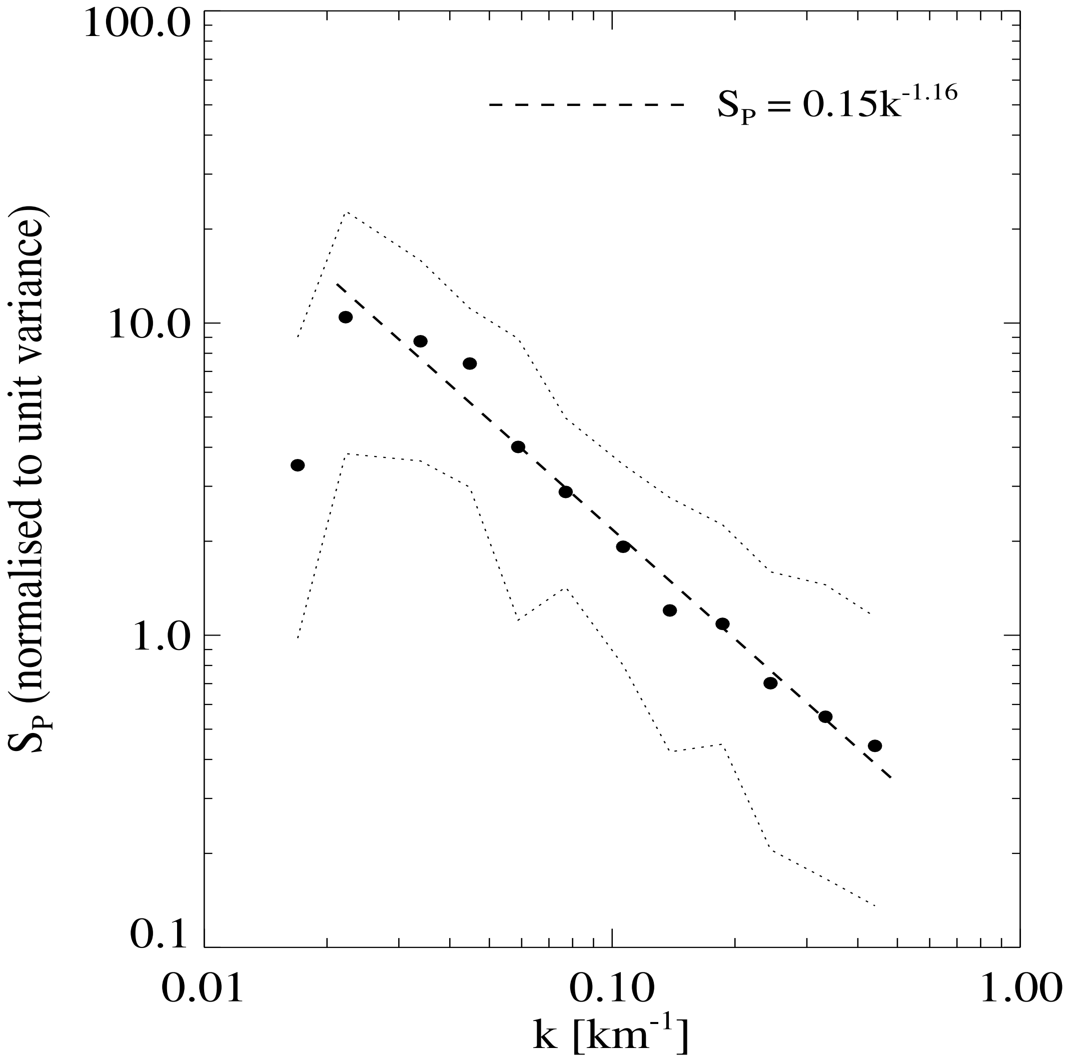

Figure 13: Composite normalised power spectrum of precipitation rate from all in-cloud and sub-cloud runs. The dotted lines show the 25th and 75th percentiles. The dashed line shows the best fit power law. Each contributing spectrum was first normalised with its variance before compositing.

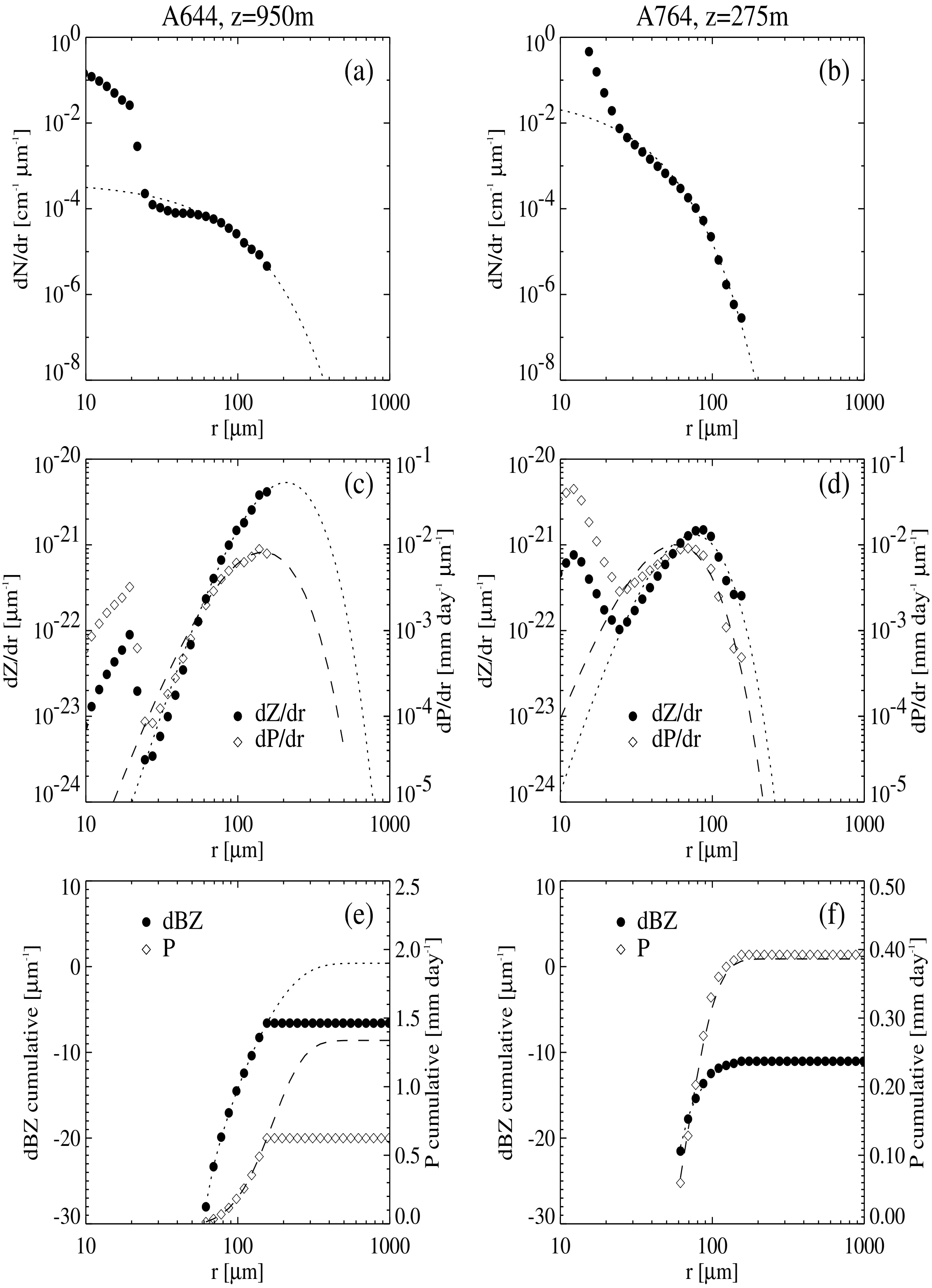

Figure 14: Examples from two flights showing drop size distributions (a,b), size resolved radar reflectivity dZ/dr and precipitation rate distributions dP/dr (c,d) and the cumulative values of dBZ integrated from $r = 60\mu$m upwards. Data values obtained using the 2D-C and FSSP probes are shown using symbols, and dashed and dotted lines show the fitted exponential distributions. For the $z = 950$ m run in flight A644 (left) the exponential distribution suggests that both P and R have contributions from drops larger than those actually measured. For the $z = 275$ m run in A764 the measurements capture almost entirely the contributions to P and R.

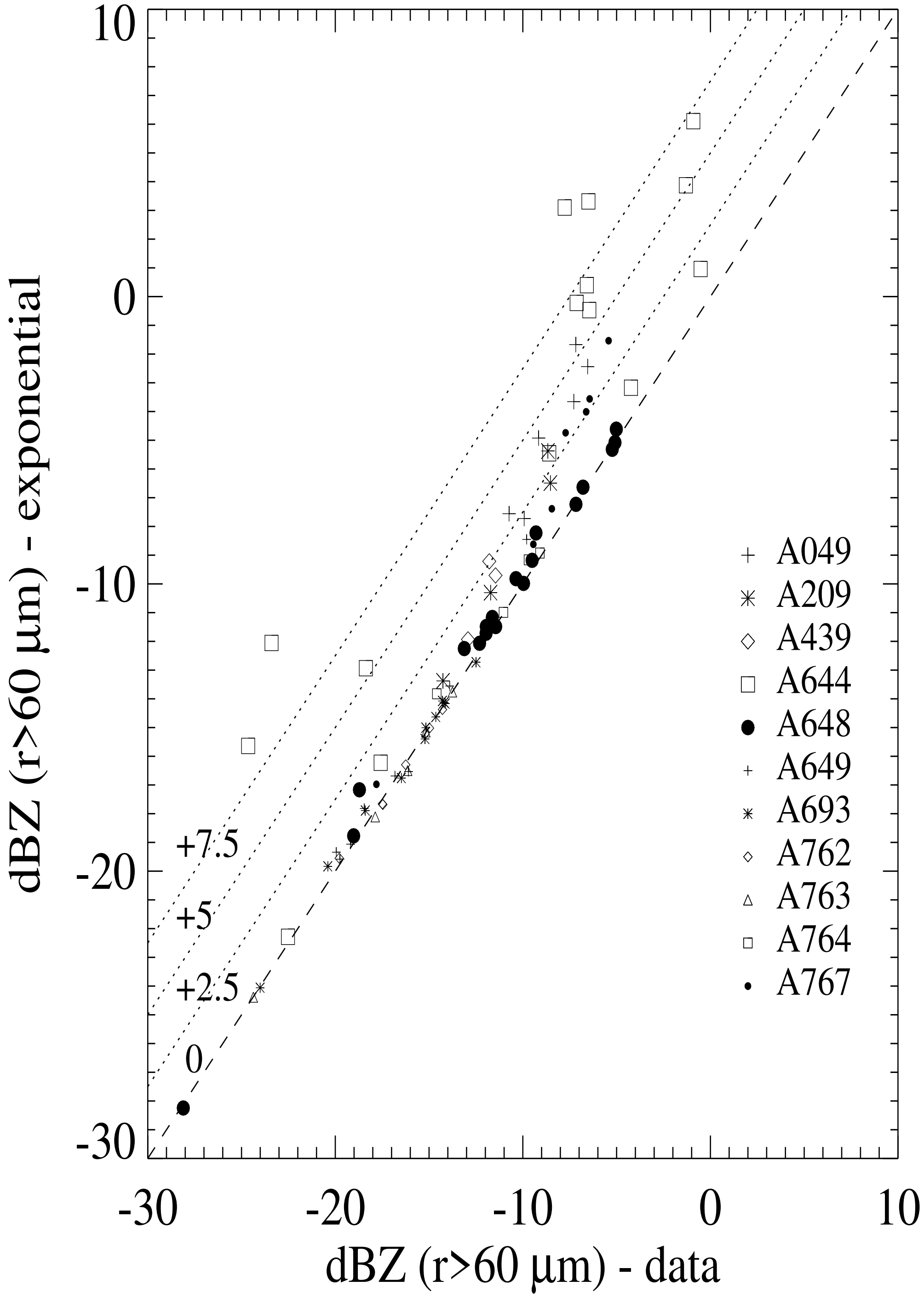

Figure 15: Reflectivity factor dBZ derived using droplets with radii larger than 60 μm for data values (abscissa) and for the fitted exponential distributions extrapolated to $r = \infty$ (ordinate). In most cases there is only a small difference between the two values indicating that the 2D-C sample volume is sufficiently large enough to account for significant contributions to reflectivity from all droplet sizes. However, in A644 there are differences of at least 10 dBZ in some cases which arise because drops larger than those measured using the 2D-C are contributing significantly to the reflectivity.

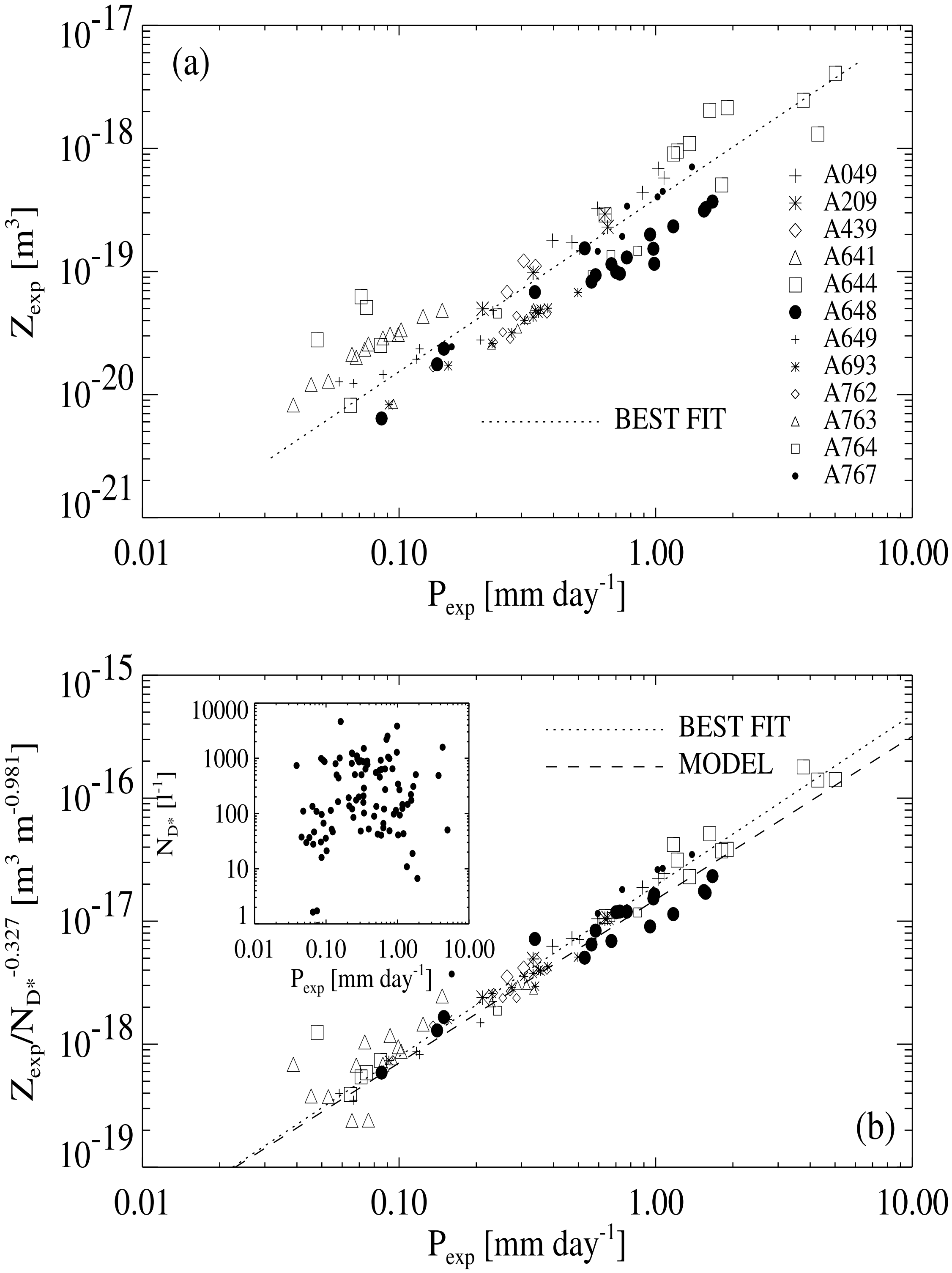

Figure 16: (a) Derived reflectivities Z_{exp} plotted against precipitation rates P_{exp} for all the in-cloud extrapolated distributions. The dotted line represents the best fit power law with parameters given in Table 5; (b) Values of $Z_{exp}/N_{d,D}^{1-6/(3+d)}$ for the extrapolated cases plotted against P_{exp} for the same cases. The dotted line shows the best fit and the dashed line shows the result from a model that assumes an exponential size distribution (see text). Inset shows that there is not a particularly good correlation between precipitation rate P_{exp} and exponential drizzle drop concentration N_{D*}.

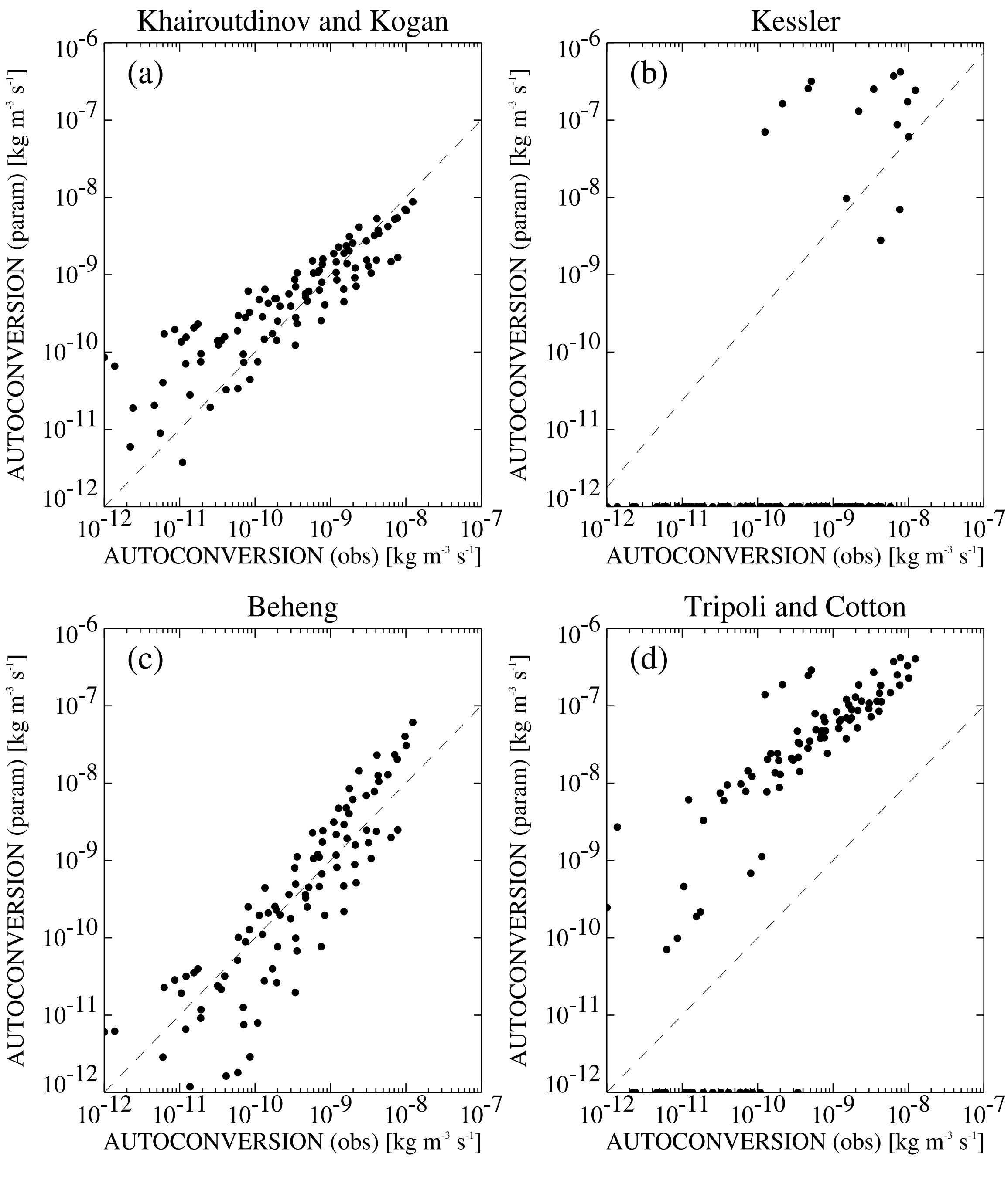

Figure 17: Comparison of autoconversion rates derived from the observed droplet size distributions (abscissae) and from the parameterizations of (a) Khairoutdinov and Kogan (2000); (b) Kessler (1960); (c) Beheng (1994); (d) Tripoli and Cotton (1980). Formulations for the parameterized autoconversion rates are presented in Table 6. Points for which the parameterized autoconversion rates are zero are shown along the abscissae.

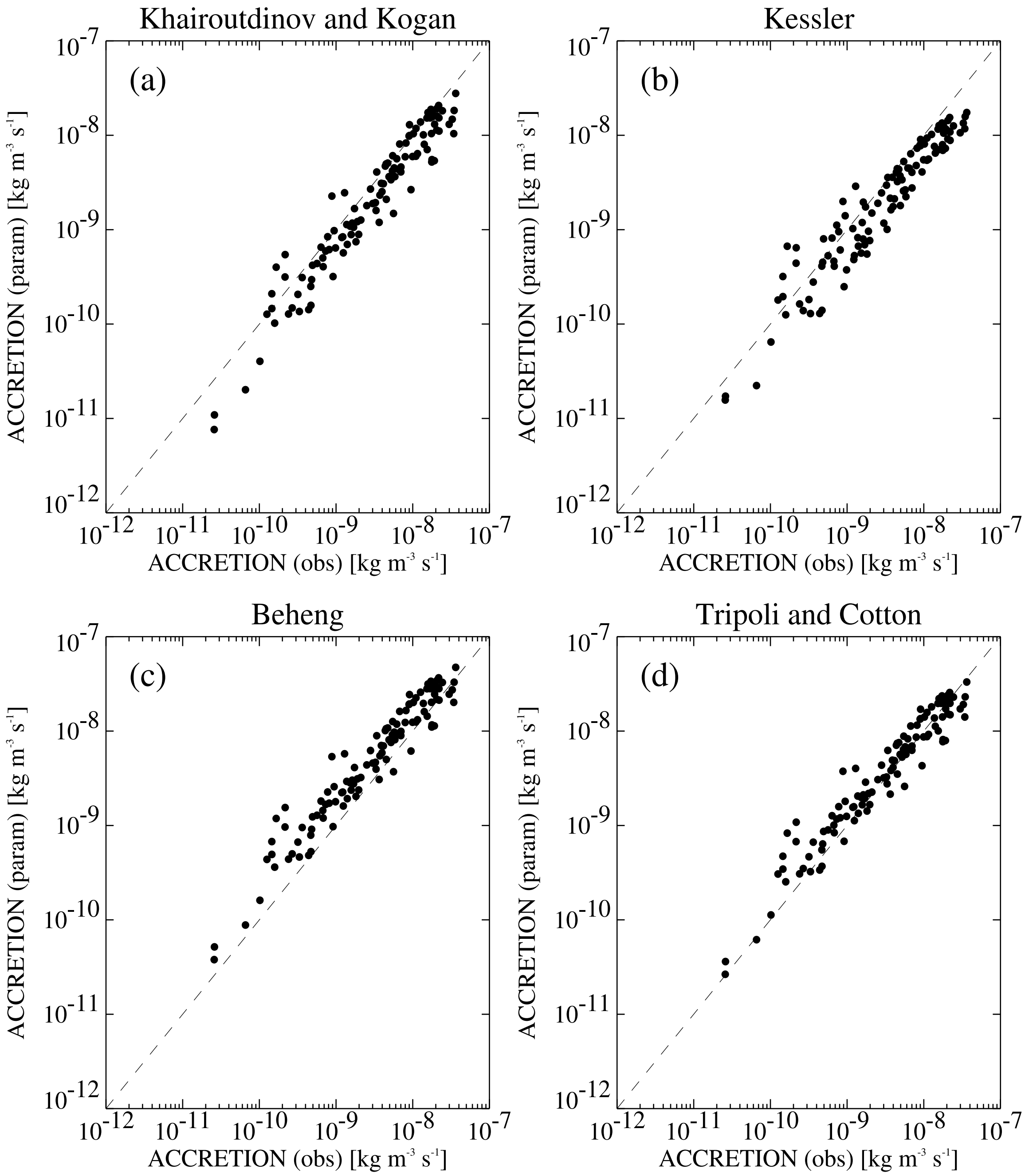

Figure 18: As for Fig. 17 but comparing accretion parameterizations.

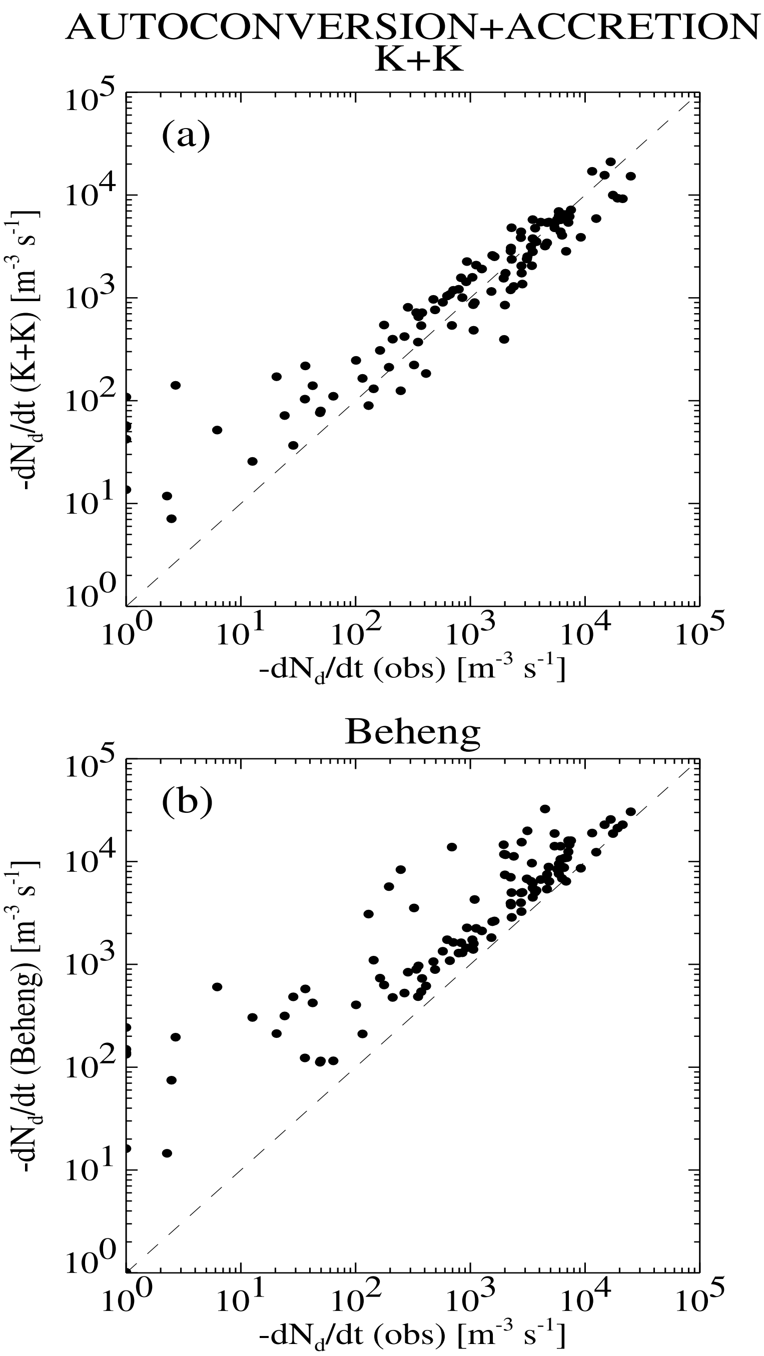

Figure 19: Comparison of combined autoconversion/accretion rate of loss of cloud droplets derived from the observed droplet size distributions (abscissa) with those parameterized (ordinate) assuming that all collected drops have the size of the mean volume radius of the cloud drops r_v.

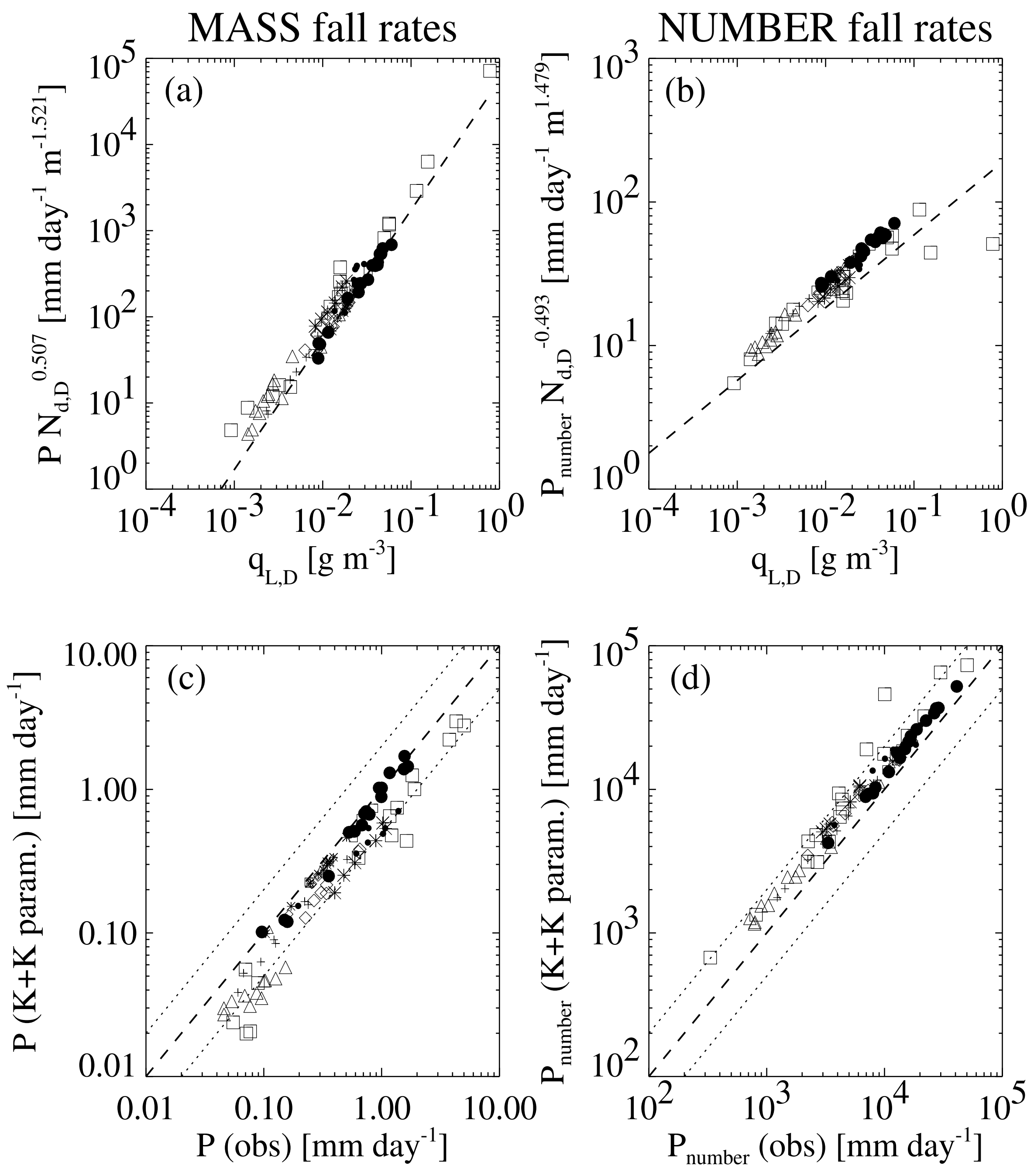

Figure 20: Mass (left) and number (right) fall rates as defined in Eqns. 2 and 12. The upper two plots show the mass (a) and number (b) fall rates from observations normalised with the $r > 20\mu$m drizzle droplet concentration $N_{d,D}$ to a power obtained using the exponential formulations of Eqns. 15 and 16 against the $r > 20\mu$m drizzle drop mass $q_{L,D}$. The dashed lines show the exponential model. The lower two plots show the mass (c) and number (d) fall rates compared with those using the parameterization of Khairoutdinov and Kogan (2000). Dashed lines show perfect agreement; dotted lines show factor of two errors. Symbols are as Fig. 15.